2020-02

The development of a 3D computational mesh to improve the representation of dynamic processes: The Black Sea test case

Bruciaferri, Diego

10.1016/j.ocemod.2019.101534
Ocean Modelling
Elsevier

Ocean Modelling 146 (2020) 101534

Contents lists available at ScienceDirect

Ocean Modelling

journal homepage: www.elsevier.com/locate/ocemod

The development of a 3D computational mesh to improve the representation of dynamic processes: The Black Sea test case

Diego Bruciaferri [a,*], Georgy Shapiro [a], Sergey Stanichny [b], Andrey Zatsepin [c], Tal Ezer [d], Fred Wobus [a], Xavier Francis [a], Dan Hilton [a]

[a] University of Plymouth, Faculty of Science and Engineering, Plymouth Ocean Forecasting Centre, Drake Circus, Plymouth, Devon, PL4 8AA, UK
[b] Marine Hydrophysical Institute, Sevastopol, Kapitanskaya St., 2, Ukraine
[c] Shirshov Institute of Oceanology Russian Academy of Sciences, 36 Nahimovski ave., Moscow, 117997, Russia
[d] Old Dominion University, Center for Coastal Physical Oceanography, 4111 Monarch Way, Norfolk, VA 23508, USA

ARTICLE INFO

Keywords:
Ocean modelling
Vertical coordinate
Curvilinear grid
Black Sea

ABSTRACT

The Black Sea is one of the largest land-locked basins in the world. Due to the vulnerability of its unique marine ecosystem, accurate long-term modelling of its hydrodynamics is needed. In this study, we first compare the skills of four NEMO based Black Sea models in a free-run which use different discretization schemes. We find that the most accurate results are obtained with the model (named CUR-ME*s*) which has a 3D mesh optimized for the prevailing dynamics. This new model uses a curvilinear horizontal grid with increased resolution (≈ 950 m) over the shelf-break and lower resolution (≈ 6 km) in areas where the scale of relevant processes is larger (≈ 20 km). In the vertical, CUR-MEs uses Multi-Envelope curved s-levels designed to optimize the representation of the Cold Intermediate Layer (CIL). Second, we compare CUR-MEs in free-run with the data-assimilative CMEMS reanalysis. Validation against independent observations shows that the two models have similar skills - e.g., the difference between the mean BIAS and RMSE of the two models is $\approx 0.15°C$ for temperature and ≈ 0.07 for salinity. The CUR-MEs model, even without data assimilation, is able to correctly reproduce the details of the variability of the Mean Kinetic Energy and the CIL.

1. Introduction

The Black Sea is one of the largest land-locked basins in the world, located on the border between Europe and Asia. It communicates with the Mediterranean sea via the Marmara and Aegean seas and through a system of narrow straits, namely the Bosphorus and the Dardanelles (Shapiro, 2008).

In 2004, the population of states bordering the Black Sea counted a total of about 294 million inhabitants (Vespremeanu and Golumbeanu, 2018), making the coastal and shelf zones of the sea areas of prime economical and social importance (Shapiro et al., 2011). During the end of the last century, the increased Black Sea anthropogenic pollution caused one of the worst environmental crises of the world oceans, resulting in the collapse of much of its coastal ecosystem (Mee, 1992).

One of the most defining feature of the Black Sea circulation is the Rim Current, a basin-scale coherent cyclonic current flowing in a proximity of the shelf-break (Shapiro et al., 2010). The Rim Current is a subject to instabilities which eventually lead to the generation of mesoscale anticyclonic coastal eddies (Staneva et al., 2001; Shapiro, 2008). Mesoscale eddies contribute to shelf-deep sea water exchanges and hence to the health of the marine ecosystem (e.g., Zatsepin et al. (2003), Shapiro et al. (2010), Zhou et al. (2014) and Stanev et al. (2014) and references therein).

A specific thermal feature of the Black Sea is the Cold Intermediate Layer (CIL), a distinct well preserved sub-surface water mass with temperature minimums located between the seasonal and permanent pycnoclines (e.g., Ivanov and Belokopytov (2012) and references therein). The CIL separates the Black Sea oxygen-rich surface layer from the oxygen-depleted deeper waters contaminated with the hydrogen sulphide. Recent studies indicate a weakening of the CIL (e.g. Capet et al. (2016)), which could result in greater mixing between deep and surface water with potential catastrophic consequences for the biota. Hence there is a need for accurate long-term modelling of the Black Sea marine environment including the variability of the CIL, trends in its circulation and other parameters underpinning the state of its ecosystem.

Several Black Sea ocean models exist, the majority of which combines a regular geographical horizontal grid with a constant resolution, with one of the standard vertical coordinate systems, either z-level (geopotential) or terrain-following (see Stanev (2005) for a review of different coordinate systems used in the Black Sea modelling). For

* Correspondence to: Met Office, Exeter, EX1 3PB, UK.
E-mail address: diego.bruciaferri@metoffice.gov.uk (D. Bruciaferri).

https://doi.org/10.1016/j.ocemod.2019.101534
Received 17 May 2019; Received in revised form 12 November 2019; Accepted 24 November 2019
Available online 29 November 2019

example, z-level coordinates are used in the studies by Staneva et al. (2001), Korotaev et al. (2011) and many others. Terrain-following coordinates were used, among others, by Besiktepe et al. (2001) and Cannaby et al. (2015).

Neither of these two discretization schemes are free of errors (Griffies, 2004). In z-coordinate systems, the step-like representation of the bottom topography leads to overmixing over the continental slope while terrain-following models are known to have errors in computing the pressure gradient force, particularly in areas of steep continental slope (e.g. Ezer and Mellor (2004)). Moreover, both vertical discretization methods are affected by the spurious numerical diapycnal mixing when computational surfaces cross the isopycnals. Vertical grids where computational levels follow isopycnals (known as isopycnal grids, e.g. Bleck (1998)) have their own disadvantages, especially in weakly stratified areas, such as over the continental shelf or in the upper or bottom mixed layers (Griffies, 2004).

In order to minimize above mentioned computational errors, several methods were developed. For instance, Grayek et al. (2010) and Ciliberti et al. (2016) used a z-levels with a partial steps vertical discretization scheme (Pacanowski et al., 1998) to overcome the problems of z-models when reproducing the bottom topography. Regarding terrain-following models, several different methods were developed to reduce the horizontal pressure gradient errors and improve their accuracy in the Black Sea. Stanev and Beckers (1999b) and Capet et al. (2012) used a model with the double-sigma vertical coordinate system to study barotropic and baroclinic oscillations and the long term variability of the Black Sea physical processes. Enriquez et al. (2005) showed that using an artificial flat bottom at a depth of 1500 m to reduce the curvature of the terrain-following coordinate system allows to adequately reproduce the mesoscale circulation of the sea. Shapiro et al. (2013) introduced a novel s-on-top-of-z vertical discretization scheme able to combine the advantages of both $z-$ and $s-$level schemes and, therefore, minimize their drawbacks. Recently, Miladinova et al. (2017) proved that a generalized boundary-following vertical grid can be used to study the long-term variability of the Black Sea thermohaline properties.

Regarding the horizontal discretization, two main approaches are used in high-resolution ocean modelling: (i) nesting the high-resolution model into a lower-resolution one, and (ii) using a horizontal grid with variable resolution. For example, Diansky et al. (2013) and Gusev et al. (2017) used a structured horizontal grid (i.e. with trapezoidal cells) with increased resolution ($\approx$ 50 m) near the Big Sochi coast to improve the simulation of oil spills. Divinsky et al. (2015) used unstructured grids with triangular cells to study the sub-mesoscale dynamics of the Black Sea northeastern shelf. Recently, Stanev et al. (2017) used an unstructured grid combining triangular and quadrilateral cells with an increased resolution in the Kerch, Bosphorus and Dardanelles straits to study the circulation and interbasin exchange in the Azov–Black–Marmara–Mediterranean Seas system.

A widely used method to improve model skills is Data Assimilation (DA). Whilst there is an abundance of the sea surface data, such as temperature or sea level anomalies obtained by the satellites, in situ observations of the water column are much scarcer. Therefore, there is a need for a model able to generate smaller errors in free-run (without DA), hence requiring less observational data.

The aim of this study is to assess and quantify whether optimizing the 3D computational mesh of a Black Sea model for the prevailing physical processes in question has an impact on the accuracy of the simulation. For that reason, we investigate the behaviour of four numerical models of the Black Sea hydrodynamics based on NEMO 3.6-stable ocean code (Madec, 2008). All models have the same initial condition and external forcing, while they differ in the combination of the horizontal and vertical discretization schemes. Two different types of numerical experiments are carried out. In the first experiment, the modelling skills of all four simulations are compared, in order to identify the one with the best accuracy. In the second one, the simulation showing the best behaviour is compared to the EU (CMEMS) Black Sea reanalysis dataset. CMEMS is a data-assimilating system that currently represents the best official EU estimate of the 1995–2015 Black Sea state. Finally, we investigate the seasonal and interannual variability of the Mean Kinetic Energy (MKE) and the CIL simulated by the model with the highest accuracy in the first experiment and the CMEMS reanalysis.

Table 1
Features of the numerical mesh of the four Black Sea models developed in this study. The CUR-MEs model, which is the model showing the best accuracy in the first experiment (see Section 3.1), is highlighted in bold. The resolution of the vertical grids is computed in the deep basin.

Model	Horizontal grid type	Horizontal resol. [m]	Vertical grid type	Vertical resol. [m]
GEO-*zps*	Regular Geograph. (GEO)	min = 2757 max = 3035 mean = 2908	z-coord.+ part. steps (zps)	min = 1 max = 176 mean = 44
GEO-MEs	Regular Geograph. (GEO)	min = 2757 max = 3035 mean = 2908	Multi-Env. s-coord. (MEs)	min = 1 max = 171 mean = 42
CUR-*zps*	Shelf-break following (CUR)	min = 984 max = 6172 mean = 2646	z-coord.+ part. steps (zps)	min = 1 max = 176 mean = 44
CUR-MEs	**Shelf-break following (CUR)**	**min = 984 max = 6172 mean = 2646**	**Multi-Env s-coord. (MEs)**	**min = 1 max = 171 mean = 42**

The paper is organized as follows. Section 2 describes in detail the four numerical models implemented in this study (Section 2.1), the design of the performed numerical experiments (Section 2.2), the external datasets used to validate or to compare with the models' results (Section 2.3) and metrics used to assess the models' accuracy (Section 2.4). In Section 3, numerical results of the first and second experiments are presented and discussed in Sections 3.1 and 3.2, respectively, while in Section 3.3 we analyse the variability of the MKE of the geostrophic currents and the CIL simulated by the new model and the CMEMS reanalysis. Section 4 summarizes our main conclusions.

2. Materials and methods

In this study, we simulate the Black Sea hydrodynamics by using a modified version of NEMO General Circulation model (Madec, 2008) along with real external forcings. The governing equations solved by the NEMO ocean model together with parameters and numerical techniques adopted in this study are detailed in Appendix.

2.1. Numerical model setups

Four numerical models are implemented differing only in the type of the 3D mesh. In the horizontal direction the models use (i) a regular geographical horizontal grid (hereafter called GEO) or (ii) a shelf-break following curvilinear grid (hereafter called CUR) where grid lines are designed to follow the 200 m isobath. In the vertical, the models use (i) a standard z-levels with partial steps discretization scheme (hereafter called zps) or (ii) the new Multi-Envelope s-coordinate system of Bruciaferri et al. (2018) (hereafter called MEs). The four numerical models are identified in the paper as GEO-zps, GEO-MEs, CUR-zps and CUR-MEs and their features are summarized in Table 1.

2.1.1. Models' domain

The models' domain covers the entire Black Sea, from 27.4°E to 41.9°E in the zonal direction and from 40.8°N to 46.7°N in the meridional one (Fig. 1a). The current implementation considers closed lateral boundaries and the Bosphorus exchanges are parameterized by a two-layer river.

The bottom topography dataset used in this study is taken from the high-resolution EMODnet Digital Topography Model 2018 (Shom,

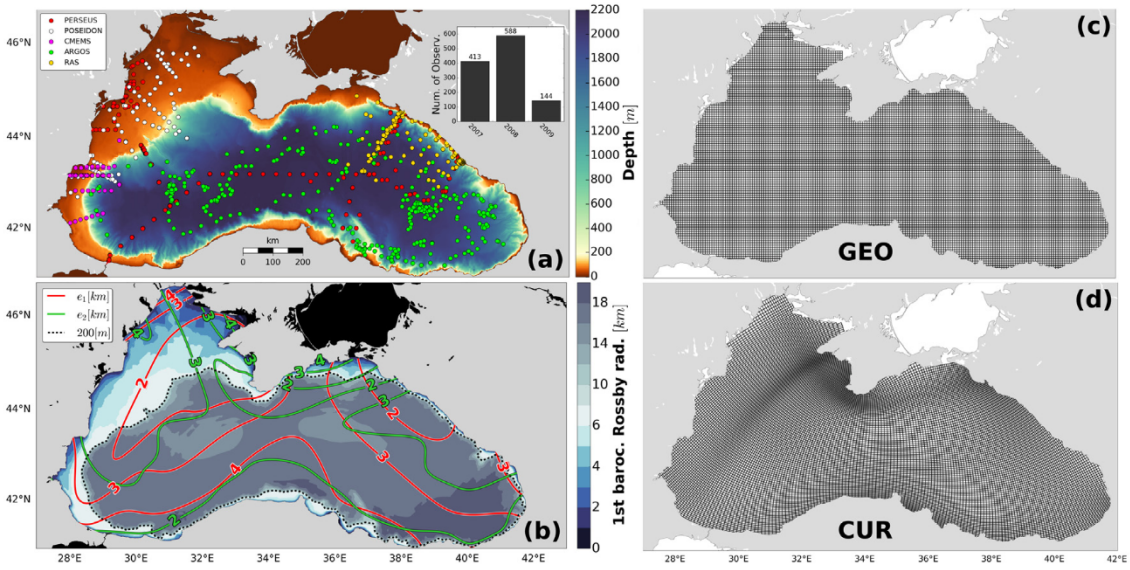

Fig. 1. (a) EMODnet DTM 2018 Black Sea topography map and locations of hydrographic stations (see Section 2.3) used to validate models results. In the inset, the histogram shows the total number of observations available for each year. (b) Map of the first baroclinic Rossby radius of deformation R_D in the Black Sea and CUR horizontal grid resolution (e_1 and e_2 are grid cells sizes in km). (c) Map of the regular geographical grid GEO and (d) map of the orthogonal curvilinear grid CUR developed for this study. Grid nodes are plotted every 2 points in each direction for clarity.

2018) (Fig. 1a). Models' bathymetry is computed by averaging all the EMODnet topography points within a particular wet cell of the models' grid. Such an approach allows one to create a remapped lower resolution bathymetry which is highly representative of the finer resolution one, especially in the regions where steep bathymetry changes occur (Sikirić et al., 2009). The minimum depth of the models bathymetry is 6 m while the maximum is 2208 m.

2.1.2. Horizontal grids

Two different horizontal grids with the same number of grid points 405×225 are implemented. The first one is a regular geographical grid with grid lines aligned with parallels and meridians, with a resolution of $\approx$ 3 km in both directions and denoted as GEO in the manuscript (Fig. 1c).

The second one is a general orthogonal curvilinear grid and it is identified as CUR in the paper (Fig. 1d). It is designed to have grid lines following the shelf-break line (the 200 m isobath) with a variable grid cells sizes and higher resolution near the shelf-break. The minimum grid size of the CUR grid is $\approx$ 1 km, while its maximum value is $\approx$ 6 km.

The generation of horizontal general curvilinear grids involves the usage of a 2D conformal transformations which allows mapping of an irregular physical domains with physical coordinates (x, y) onto regular computational domains with orthogonal coordinates (i, j) (Ives, 1982).

In order to better resolve mesoscale and sub-mesoscale dynamics, the CUR grid has an increased resolution in a proximity of the 200 m isobath, especially along the cross shelf-break direction. This approach should allow to:

1. improve the accuracy of the simulations regarding the interactions between the meso-scale eddies and the large-scale circulation, since the first baroclinic Rossby radius of deformation R_D is resolved more accurately;
2. reduce horizontal pressure gradient errors arising from the discretization of the governing equations with curved vertical levels, since the slope parameter is reduced, i.e. the change of depths of adjacent grid points divided by their mean (e.g. Ezer and Mellor (2000));
3. have a more realistic (in terms of resolution) bathymetry in a proximity of the shelf-break and hence a more accurate simulation of the influence of the topography on the oceanic flow;

Fig. 1b describes the relationship between the first baroclinic Rossby radius of deformation R_D in the Black Sea and CUR grid resolution (e_1 and e_2 are grid cells sizes, see Appendix). The Black Sea Rossby radius of deformation is computed as

$$R_D = \frac{c_1}{|f|} \tag{1}$$

where $f = 2\Omega \sin\theta$ is the Coriolis parameter (Ω is the Earth's angular velocity and θ is the latitude) and c_1 is the first eigenvalue satisfying the Sturm–Liouville boundary value problem for the vertical velocity of the linearized quasi-geostrophic potential vorticity equation with zero background mean flow (Chelton et al., 1998). Monthly climatological data of temperature and salinity taken from the Black Sea Atlas (Suvorov et al., 2003) are used to compute c_1. Excluding a narrow strip of very shallow areas near the coast, our calculation of R_D corresponds to an average first baroclinic Rossby radius of $\approx$ 20 km in the Black Sea, in agreement with previous estimates (e.g. Blatov and Ivanov (1992), Blokhina and Afanasyev (2003), Stanev (2005) and Zatsepin et al. (2019)). Fig. 1b shows that the CUR grid is eddy resolving, except in limited areas near the coast where the Rossby radius is very small. The grid anisotropy e_2/e_1 is ≤ 3.3 (Xu et al., 2015).

2.1.3. Vertical grids

Two different vertical grids with 51 levels are implemented in this paper (see Fig. 2): one uses the common z-level with partial steps (zps) scheme, while the second one uses the novel Multi-Envelope s-coordinate (MEs) system (Bruciaferri et al., 2018). For better comparison, both MEs and zps grids have the computational level $n°$ 36 placed at the same depth of 310 m.

The zps grid (Fig. 2a, c) uses a standard NEMO v3.6 z-partial steps scheme (Madec, 2008) with a minimum layer thickness of 1 m. Partial steps parameters are given in Appendix.

The MEs grid is configured using five envelopes (see red lines labelled H^i_e, with $1 \leq i \leq 5$, in Fig. 2b, d and f) and the same number of levels as the zps scheme (i.e. 51). Envelopes are arbitrary reference surfaces which divide the ocean model vertical domain into sub-zones D_i, with $1 \leq i \leq 5$ (see Fig. 2b and c). They are used to define computational surfaces that in each sub-zone D_i are curved and adjusted to follow boundary envelopes (see Bruciaferri et al. (2018) for the details). Our Black Sea MEs grid has 27 levels allocated to the uppermost sub-zone D_1, 6 to the intermediate sub-zone D_3 and 5 to the

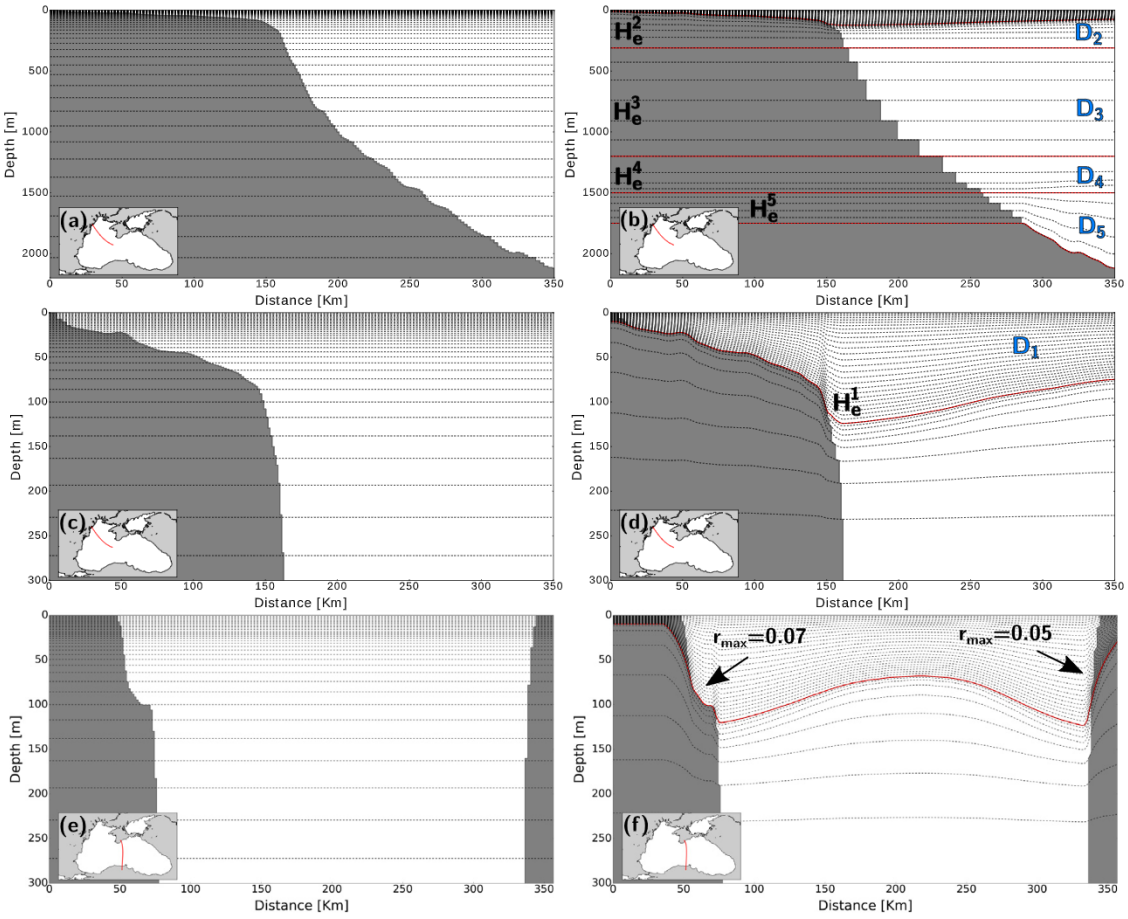

Fig. 2. Model bathymetry and computational levels configuration in the *zps* (a, c and e) and ME*s* (b, d and f) vertical grids along sections shown in the inset. Panels a, b, c and d show the same vertical transect, with c and d showing the zoomed part between the surface and 300 m depth.

deeper sub-zone D_5, while 9 and 4 computational surfaces are assigned to transition sub-zones D_2 and D_4, respectively. Envelopes H_e^2, H_e^3 and H_e^4 are geopotential surfaces located at depths of 310, 1200 and 1500 m respectively. This means that the sub-zone D_3 of the ME*s* grid is effectively discretized with z-levels. The deeper envelope H_e^5 is a smoothed version of the actual bathymetry with depths greater than 1800 m. Smoothing is performed by applying the Martinho and Batteen (2006) algorithm with a maximum slope parameter $r_{max} = 0.06$.

The origin and replenishment of the CIL is classically attributed to the mutual interaction of the two main processes (Stanev et al., 2003; Korotaev et al., 2014): the cascading of cold water formed during winter in the north-western shelf and winter convective mixing in the middle of cyclonic gyres. In order to properly represent these two physical processes, the upper envelope H_e^1 is designed to follow an 'enveloping'-bathymetry over the continental slope and shelf while it follows the climatological winter isopycnic surface with density $\sigma_e = 15.4$ kg m^{-3} in open ocean areas. Such isopycnic surface is typically used to identify the deeper boundary of the CIL (Ivanov and Belokopytov, 2012) and it is computed by using January, February and March climatological temperature and salinity data from the Black Sea Atlas (Suvorov et al., 2003).

The terrain-following portion of the envelope H_e^1 has minimum and maximum depths equal to 10 and 140 m, respectively. The envelope is obtained by smoothing the actual topography according to local criteria: the Hanning filter is applied in a proximity of the Danube canyon, while different slope parameter threshold values for the Martinho and Batteen (2006) smoothing algorithm are used in different areas of the domain. For example, in the north-western shelf a maximum slope parameter $r_{max} = 0.07$ is used, while in the south-eastern part of the domain we use $r_{max} = 0.05$ to handle a wall-like topography. When the slope parameter is higher than the prescribed r_{max}, the envelope is smoothed, resulting in computational levels going below the actual bottom (see Fig. 2f). With this approach we are able to reduce numerical errors linked to the computation of horizontal pressure gradients with curved levels without changing the model bathymetry. The thickness of the uppermost model cell in the middle of the domain is ≈ 1 m.

2.1.4. Models' initial condition and external forcings

Numerical simulations span the 2007–2009 period. This time interval was chosen due to the data availability, for both external forcings and observations (see Section 2.3). Momentum, water and heat fluxes are computed using the CORE bulk formulae (Large and Yeager, 2009) along with the atmospheric fields taken from the SKIRON weather forecasting system (Kallos et al., 1997) . The SKIRON forecast dataset has horizontal and temporal resolutions of $0.1° \times 0.1°$ and 2 h, respectively, including wind speed at 10 m, air temperature and specific humidity at 2 m, short and long wave radiation and total precipitation.

Accurate atmospheric forcing is crucial for the adequate performance of ocean models. This is especially true for the Black Sea, where small errors in the freshwater and heat forcings could result in large inaccuracies in long-term simulations of water masses formation processes (Stanev et al., 1997). In particular, cloud-related short-wave errors may cause excessive downward surface short-wave radiation, affecting the ability of a Black Sea model to properly represent the CIL interannual variability (Staneva et al., 1995).

Recently, Miladinova et al. (2018) showed that the ECMWF ERA-Interim reanalysis atmospheric dataset can be used to realistically simulate the multi-year CIL dynamics. For this reason, we weight the SKIRON short-wave radiation forcing with monthly climatological

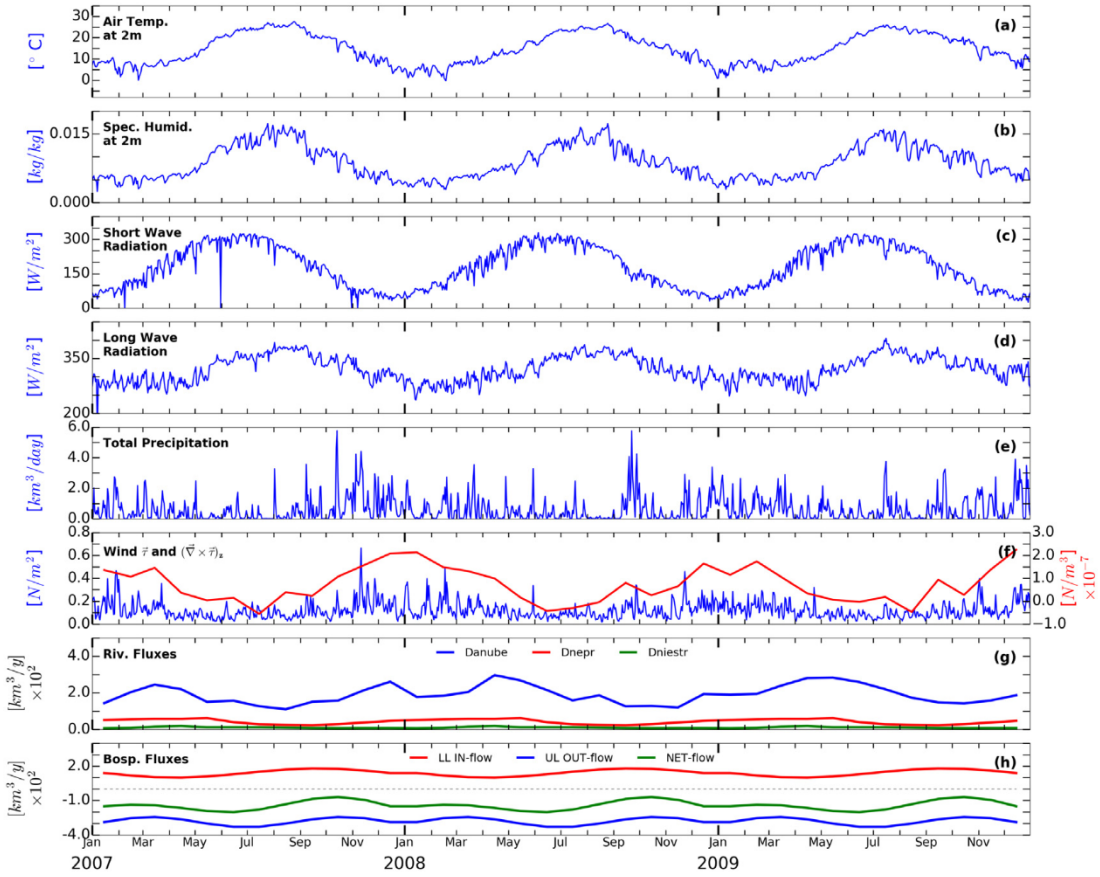

Fig. 3. (a–f) Timeseries of the basin averaged SKIRON atmospheric fields used to force the four Black Sea models: (a) Air temperature at 2m [°C]; (b) Specific humidity at 2m [kg/kg]; (c) Short wave radiation [W m^{-2}]; (d) Long wave radiation [W m^{-2}]; (e) Total precipitation [km^3 day^{-1}]; (f) Wind stress $\vec{\tau}$ (blue line) [N m^{-2}] and wind stress curl $(\vec{\nabla}\times\vec{\tau})_z$ (red line) [N m^{-3}]. (g) Monthly timeseries of the river discharges [km^3 year^{-1}] of Danube (black), Dnepr (red) and Dniester (blue) rivers; (i) Bosphorus fluxes in the upper (blue) and lower (red) layers, while the net flux is shown in green. Negative values identify flows from the Black Sea to the Marmara sea.

factors. They are determined by fitting the area averaged SKIRON shortwave signal with the one from the ERA-INTERIM reanalysis. Panels a, b, c, d, e, f in Fig. 3 present timeseries of the basin averaged SKIRON atmospheric fields used in this study, showing that the seasonal variability and the magnitude of the atmospheric forcing are in good agreement with previous estimates (e.g. Stanev et al. (1995) and Miladinova et al. (2018)).

The models contain 11 main rivers and river discharges are estimated by approximating monthly data from the Global Runoff Data Centre (GRDC, 2014). For the Danube we use daily data for 2007 and 2008 while for 2009 we use monthly climatological values. For all the other rivers, daily or monthly data are not available for the period of our study so we use monthly climatological values computed using the entire GRDC dataset. Rivers' salinity is 1. Timeseries of the river discharges for the main rivers of the Black Sea used in this study are shown in Fig. 3g.

The Bosphorus strait is characterized by a two-layer exchange system: an upper current transports low salinity water from the Black Sea towards the Marmara Sea while a deeper flow runs in the opposite direction pouring high salinity water of Mediterranean origin into the Black Sea. Upper and lower layer climatological fluxes are estimated approximating monthly values given by Aydoğdu et al. (2018) (see their Fig. 14b) with two analytical functions (see blue, red and green lines in Fig. 3h for upper layer out-flow, lower layer in-flow and net-flow, respectively). Salinity of incoming Mediterranean water is set to 36.

Our models have closed lateral boundary conditions and volume conservation is ensured redistributing the excess or deficit of water flux between surface model cells according to their corresponding area. (see Appendix for the details).

All numerical experiments start from the 15th of January 2007. The model is initialized as follows. The initial condition for Temperature and Salinity (T/S hereafter) is obtained by using January climatological data from the Black Sea Atlas. Climatological data from the Black Sea Atlas are estimated by using observations collected in the period 1960–1995 (Suvorov et al., 2003). Then, the matching initial velocities are obtained with the 'semi-diagnostic adjustment' method (Ezer and Mellor, 1994; Enriquez et al., 2005), i.e. running the model for one year without any external forcing and not allowing the evolution in time of the T/S initial fields. Fig. 4a shows the evolution in time of the basin averaged Kinetic Energy (KE) of the four models during the semi-diagnostic adjustment runs. After 150−180 days, all models show a stationary basin averaged KE, indicating that 5 − 6 months is the period needed for the models to reach a state of a physical equilibrium.

After the models have been initialized, numerical experiments are run in a fully prognostic 'free' mode, without any DA or relaxation to the climatology. Fig. 4b presents the timeseries of the monthly basin averaged wind stress curl and the daily basin averaged KE of the upper 200 m of the water column of GEO-*zps* and CUR-ME*s* models (the ones of CUR-*zps* and GEO-ME*s* are very similar and are not shown here for clarity). In agreement with the semi-diagnostic adjustment runs, after 5 months of simulation the barotropic wind-generated ocean dynamics of the four models is fully adjusted to the atmospheric forcing. Therefore, the first 5 months of the simulations are considered as a spin up period and numerical results are analysed starting from 01 June 2007.

2.2. Experimental design

Two different types of numerical experiments are carried out. In the first experiment (hereafter EXP-1), the modelling skills of the four

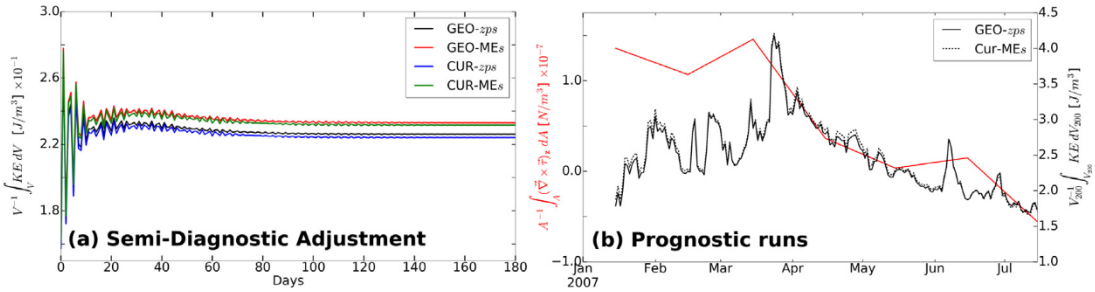

Fig. 4. (a) Daily timeseries of the basin averaged KE [J m^{-3}] of GEO-*zps* (black), GEO-ME*s* (red), CUR-*zps* (blue) and CUR-ME*s* (green) models for the semi-diagnostic adjustment runs. (b) Timeseries of the monthly basin averaged SKIRON wind stress curl $(\vec{\nabla}\times\vec{\tau})_z$ [N m^{-3}] (red line) and the daily basin averaged KE of the upper 200 m of the water column of GEO-*zps* (black continuous line) and CUR-ME*s* (black dashed line) models. The timeseries of the basin averaged KE of CUR-*zps* and GEO-ME*s* models are not shown for clarity, being very similar to the ones of GEO-*zps* and CUR-ME*s*, respectively.

models implemented in this study are compared in (i) an initial test to assess the generation of spurious currents and (ii) a realistic simulation of the Black Sea hydrodynamics. The 90 day long initial test starts from a horizontally uniform T/S distribution and zero velocity, with no river discharges, no exchanges via the Bosphorus and no meteorological forcing. In such conditions the current velocities should remain zero, and any emerging currents should be attributed to the model errors. The realistic simulations are carried out from the 15th of January 2007 to the 31th of December 2008 and numerical results are validated against a number of observational datasets detailed in the next section. All simulations are carried out in a 'free-run' mode, without DA or relaxation to climatology. The aim of this series of simulations with a progressive increase of realism is to investigate the effect of a particular combination of horizontal and vertical discretization schemes on the accuracy of the simulation and to identify the model with the highest accuracy.

In the second experiment (hereafter EXP-2), we simulate the Black Sea circulation from the 15th of January 2007 to the 31st of December 2009 with the CUR-ME*s* model, which resulted to be the model with the best accuracy in EXP-1 (see Section 3.1). Then, we validate the numerical results of our CUR-ME*s* model and data from the CMEMS reanalysis against a number of observational datasets and we compare the skills of the two models. The CMEMS reanalysis can be considered as the state-of-the-art operational system for the Black Sea. Since the CMEMS reanalysis uses DA, we concentrate our analysis on comparison with independent data sets not used in the DA. The aim of this experiment is to determine whether an optimal discretization scheme and hence a better representation of physical processes in a non-assimilating model can achieve similar or better skill than those shown by a good assimilation model which uses existing standard techniques.

After comparing the accuracy of the two modelling systems against available observations, the new CUR-ME*s* model and the CMEMS reanalysis are used to investigate the 2007–2009 Black Sea variability of the Mean Kinetic Energy (MKE) of geostrophic currents and CIL properties.

2.3. External datasets used for validation or comparison

Six independent datasets are used to validate the numerical results. They include five datasets of T/S measured profiles and one dataset of gridded Sea Surface Temperature (SST). In this paper, the five hydrographic datasets are named as Perseus, Poseidon, CMEMS-Black Sea, Argo and RAS while the SST dataset is named OSTIA.

The *Perseus* dataset includes T/S observational profiles collected in the period 2007–2009 in the course of Perseus project (Crise et al., 2015). Profiles were sampled by using CTD and Niskin bottles. In total, the dataset contains 370 T/S profiles (they are represented with red circles in Fig. 1a): 40 CTD and 17 Niskin bottles profiles in 2007, 162 CTD and 101 Niskin bottles profiles in 2008 and 50 T/S profiles from Niskin bottles in 2009. The dataset covers the north-western shelf, the deep basin, the Bosphorus area and north-eastern part of the Black sea.

The *Poseidon* dataset includes 124 CTD T/S profiles. They were measured during the POS 363 RV 'Poseidon' oceanographic cruise (Friedrich et al., 2008) carried out from March 7 to 25 2008 at the Black Sea north-western shelf, in Romanian waters (see white circles in Fig. 1a).

The *CMEMS-Black Sea* dataset includes T/S profiles collected during the period 1990–2015 by the national observing systems operated by the Black Sea GOOS members, by scientific cruises from SeaDataNet NODCs and by main global networks (Marinova and Valcheva, 2017). In this paper we use a total of 62 CTD profiles measured in the south-western shelf of the Black Sea (see purple circles in Fig. 1a). Observations cover the whole of the 2007–2009 period, and they include 13 measurements in 2007, 45 in 2008 and 4 in 2009.

The *Argo* dataset (Argo, 2018) contains a total of 295 T/S profiles measured by the argo floats deployed in the Black Sea for the period 2007–2009. The dataset covers the deep basin of the Black Sea (see green circles in Fig. 1a) and includes 138 profiles in 2007, 100 in 2008 and 57 in 2009.

The *Russian Academy of Science* (RAS) dataset is obtained from a number of Russian national research projects operating in the Black Sea and collecting T/S profiles with the CTD over the period 2007–2014. In this study we use a the total number of 294 observations (see yellow circles in Fig. 1a), 205 in 2007, 56 in 2008 and 33 in 2009.

The *Operational Sea surface Temperature and sea Ice Analysis* (OSTIA) dataset (Donlon et al., 2012) is used to validate the SST of CUR-ME*s* and CMEMS. It is a freely available high resolution analysis of the global ocean SST produced at the UK Met Office by combining satellite and in-situ SST observations. The accuracy (RMSE) of the OSTIA SST product is 0.57 °C with zero BIAS (Donlon et al., 2012). In this paper we use daily maps.

In EXP-2 we compare the accuracy of our CUR-ME*s* 'free-running' model with the one of the Copernicus Marine Environment Monitoring Service (CMEMS) Black Sea Physical Reanalysis dataset.

The CMEMS reanalysis covers the period 1995–2015 and are produced by the Centro Euro-Mediterraneo per i Cambiamenti Climatici (CMCC) institute (Lemieux-Dudon et al., 2018). The numerical ocean model used by the CMEMS Reanalysis system is based on NEMO version 3.4 hydrodynamic code (Madec, 2008) and it implements a regular geographical horizontal grid with zonal and meridional resolutions of ≈ 3 km while it uses 31 z-levels with partial steps in the vertical direction (Ciliberti et al., 2016). Bathymetry is based on GEBCO dataset. Three-hourly atmospheric fields from the ECMWF ERA-Interim atmospheric reanalysis and precipitation fields from GPCP rainfall monthly dataset are used to force the model. River discharges are estimated by using monthly mean dataset provided by SESAME project while Bosphorus barotropic transport is computed to balance the freshwater fluxes on a monthly basis. The CMEMS reanalysis system assimilates in-situ hydrographic profiles (mostly Argo floats), along-track sea level anomalies (SLA) from all available missions and CMEMS gridded sea surface temperature (SST) observations. A Large Scale Bias Correction

Table 2
Comparison of the main characteristics distinguishing the CUR-ME*s* model and the CMEMS reanalysis.

Model	Horizontal grid type	Vertical grid type	Mesh points	Atmospheric forcing	Rivers runoff	Bathym.	Data assimil.	Type of simul.	Nemo code version
CUR-ME*s*	Shelf-break following (CUR)	Multi-Env *s*-coord. (ME*s*)	405 × 225 × 51	Skiron Forec.	GRDC dataset	EMODnet	NO	Free-run hindcast	3.6
CMEMS	Regular Geograph. (GEO)	*z*-coord. + part. steps	395 × 215 × 31	ERA-Int. Reanal. + GPCP	Sesame dataset	GEBCO	SLA, SST, T/S profiles, LSBC scheme	Reanal.	3.4

(LSBC) scheme is also applied, restoring T/S fields to their climatological values. Features of the CUR-ME*s* model and the CMEMS reanalysis are compared in Table 2.

2.4. Metrics used to assess models' accuracy

The accuracy of the four models implemented in this paper and the CMEMS reanalysis is quantified with respect to six independent external observational datasets (see Section 2.3).

Gridded T/S daily numerical outputs for the same days of the observations are bilinearly interpolated on the geographical location of each T/S observation. Then, in the case of hydrographic datasets, both observed and modelled profiles are linearly interpolated on 75 reference depths h_r, with vertical step Δh_r varying from 2.5 m in the first 100 m of the water column to 50 m for $250 < h_r \leq 1000$ m.

Modelling skill of the four models and the CMEMS reanalysis is assessed by computing the total (i.e. depth averaged) BIAS and root mean square error (RMSE) between simulated (Ψ^m) and observed quantities (Ψ^o), defined as

$$BIAS = N^{-1} \sum_{i}^{N} N_d^{-1} \sum_{k}^{N_d} (\Psi^m_{i,k} - \Psi^o_{i,k})$$

$$RMSE = N^{-1} \sum_{i}^{N} \left[N_d^{-1} \sum_{k}^{N_d} (\Psi^m_{i,k} - \Psi^o_{i,k})^2 \right]^{1/2}$$

where Ψ stands for either temperature or salinity, N is the number of available observational profiles and $N_d \leq 75$ is the total number of depths of each profile.

Recently, Lishaev et al. (2018) and Mizyuk et al. (2018) compared the accuracy of a number of reanalysis and forecasting systems of the Black Sea by computing BIAS and the RMSE for specific layers of the water column. They defined four depth layers in the upper 300 m of the Black Sea: a surface layer from 0 to 5 m, two sub-surface layers from 5 to 30 m and from 30 to 100 m, respectively, and one deeper layer with depths ranging from 100 to 300 m.

In order to better understand the effect of using a particular combination of horizontal and vertical grid with respect to the others, in EXP-1 we follow the same approach and we also calculate the BIAS and the RMSE for the same four depth layers. Metrics for layers are defined as before, but in this case N_d is the number of reference depths included in a particular depth layer.

3. Results and discussion

3.1. The effect of different discretization schemes on the accuracy of the simulations

The preliminary test of EXP-1 (see Section 2.2) revealed the development of spurious currents in all four models, although with small values. After 90 days, the maximum error is 0.001 m s^{-1} for both GEO-*zps* and CUR-*zps* models, while it is 0.008 m s^{-1} and 0.004 m s^{-1} for GEO-ME*s* and CUR-ME*s* models, respectively.

In agreement with Bruciaferri et al. (2018), these results prove the ability of the ME*s* vertical discretization scheme to reduce errors in the computation of horizontal pressure gradients to a level comparable with the one of standard *z*-levels with partial steps grids. We noted that a combination of ME*s* with the curvilinear horizontal grid (CUR-ME*s*) gives a further reduction of spurious currents as compared to GEO-ME*s* (0.004 m s^{-1} of CUR-ME*s* against 0.008 m s^{-1} of GEO-ME*s*). We attribute this improvement to the fact that the curvilinear grid aligned with the shelf-break reduces the slope parameter in the proximity of the shelf-break.

The numerical results of the 2007–2008 Black Sea circulation simulations carried out with the four models are validated against five datasets of T/S measured profiles collected during 2007–2008 in the Black Sea (see Section 2.3). The performance of the four models mostly differ in the period July–November 2008, with CUR-MEs showing consistently better results, see Fig. 5. This can be attributed to the fact that in summer (June–August) and autumn (September–November) the nearly-geostrophic Rim Current weakens, meso-scale activity in the Black Sea increases (Zatsepin et al., 2003; Ivanov and Belokopytov, 2012; Stanev et al., 2014) and the CUR-ME*s* model better resolves meso- and sub-mesoscale dynamics near the shelf break. For example, July–December 2008 averaged temperature BIAS and RMSE of GEO-*zps* model are −0.28 °C and 1.35 °C, respectively, being reduced to −0.20 °C and 1.17 °C in the case of the CUR-ME*s* model. In the case of salinity, the GEO-ME*s* model presents the lowest BIAS (0.07), while the CUR-ME*s* model has the lowest RMSE (0.34). However, improvements are less notable than the ones for temperature. The Black Sea salinity strongly depends on the large river discharges in the north-western shelf and the in-flow of salty Mediterranean water from the Bosphorus (e.g. Ivanov and Belokopytov (2012)). Hence, two-year long simulations might not be long enough to permit the development of significant differences in salinity between the models.

In order to better understand the effect of using a particular combination of horizontal and vertical grid with respect to the others, we continue the analysis by computing the BIAS and RMSE of the four models for the four depth layers defined by Lishaev et al. (2018) and Mizyuk et al. (2018). For each depth layer, we consider four metrics, BIAS and RMSE for temperature and salinity.

Numerical results show that the accuracy of the four models is notably different in the two sub-surface layers with depths between 5–30 m and 30–100 m, respectively (see Table 3). These layers represent the active portion of the Black Sea, where the CIL is formed and advected over the entire basin (Ivanov and Belokopytov, 2012) and where models' meshes differ the most.

The CUR-ME*s* model has the best accuracy in both layers. It has smaller errors for both salinity and temperature in layer 5–30 m, especially with respect to GEO-*zps* and CUR-*zps* models, which present the worst modelling skill. In layer 30–100 m, the CUR-ME*s* model presents improved accuracy for temperature in comparison to all the other models, while for salinity differences are small (≤ 0.02) and all the models seem to be equivalent.

The GEO-ME*s* model presents the second best accuracy in both layers, although with important differences with respect to the CUR-ME*s* model, especially for the temperature. Fig. 5 and Table 3 clearly show that GEO-*zps* and CUR-*zps* models have similar modelling skills, with the latter slightly worse in simulating temperature. These results seem to indicate that the usage of a CUR-type grid significantly improves the quality of the simulation only if combined with the ME*s* vertical scheme, confirming the fundamental role of the vertical grid in ocean modelling.

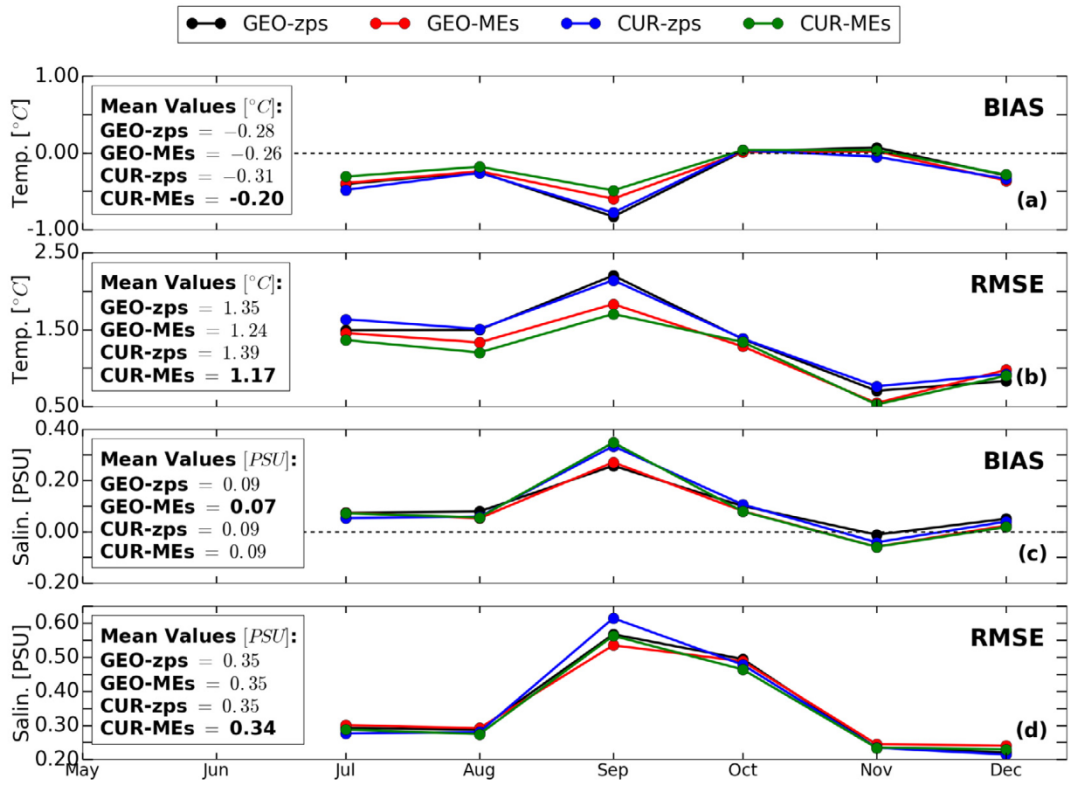

Fig. 5. 2008 summer–autumn timeseries of monthly averaged BIAS and RMSE of temperature (a and b) and salinity (c and d) profiles simulated with the GEO-*zps* (black), GEO-ME*s* (red), CUR-*zps* (blue) and CUR-ME*s* (green) models with respect to observed T/S profiles. 2008 summer–autumn averaged metrics are also given.

Table 3
2008 summer–autumn averaged temperature and salinity BIAS and RMSE of T/S profiles simulated by the four models with respect to measured T/S profiles in water column layers with depth between 5–30 m and 30–100 m.

Model	Layer 5–30 m				Layer 30–100 m			
	Salin. bias	Salin. rmse	Temper. bias	Temper. rmse	Salin. bias	Salin. rmse	Temper. bias	Temper. rmse
GEO-*zps*	0.29	0.42	−0.99	2.38	0.13	0.39	−0.28	0.91
GEO-ME*s*	0.26	0.37	−0.88	2.13	0.12	0.41	−0.28	0.90
CUR-*zps*	0.26	0.39	−1.12	2.45	0.12	0.40	−0.33	0.91
CUR-ME*s*	0.25	0.35	−0.61	1.95	0.12	0.40	−0.22	0.86

In September 2008 the modelling skills of the four models differ the most (see Fig. 5), with the CUR-ME*s* model showing the highest accuracy in simulating temperature. The basin averaged vertical profiles of the September 2008 mean BIAS (Fig. 6b) and RMSE (Fig. 6c) of the four models with respect to observations show that within the active layer 2.5 − 60 m ME*s* models present an improved accuracy (mean BIAS ≈ -0.2 °C, mean RMSE ≈ 0.5 °C) with respect to *zps* models (mean BIAS ≈ -0.3 °C, mean RMSE of ≈ 0.6 °C).

The details of the differences which lead to a better overall performance (lower RMSE and BIAS) of the CUR-ME*s* model are shown in Fig. 7a, b and c, where three examples of CTD-measured temperature profiles in September 2008 are compared with the temperature profiles simulated by the four models for the same days. Both Figs. 6 and 7 seem to indicate that the nearly isopycnal curvature of ME*s* computational levels and their increased resolution in the active layer of the sea are able to reduce the contamination of slow diapycnal mixing by fast isopycnic processes, improving the capability of the model to simulate the CIL dynamics. The differences in the RMSE of the two MEs based models (i.e. CUR-MEs and GEO-MEs) can be attributed to their different horizontal resolution — the CUR grid has a coarser resolution in the deep sea.

The difference in representing the horizontal structure of temperature distribution is shown in Fig. 8, where monthly averaged maps and transects produced by the four models in September 2008 are presented. The CIL represented in both GEO-ME*s* and CUR-ME*s* models (which have the best accuracy) is generally colder and has larger spatial extension than the one represented by the *zps* models (Fig. 8, *left column*). The CUR-ME*s* model simulates almost a homogeneous CIL with $T \leq 7.6$ °C extending from the shelf to the off-shore areas (Fig. 8, *right column*). The GEO-ME*s* model gives a similar result, although its coarser horizontal resolution on the shelf seems to increase lateral diffusion, forming CIL with $T \approx 7.9$ °C in this areas. In the GEO-*zps* model the CIL disappears over the continental slope. The CUR-*zps* model simulates the CIL on the slope but is warmer than any of the ME*s* models.

The inspection of the meridional cross-sections (Fig. 8, *middle column*) reveals that all four models are simulating cold dense water cascading in a proximity of the shelf-break. Since the ME*s* vertical grid has terrain-following levels at depths shallower than ≈ 120 m, the models using this vertical discretization scheme have higher vertical resolution in the bottom boundary layer where the cascading takes place. To the contrary, the step-like representation of the bottom topography of *zps* models seems to stop the cascading on the shelf, in agreement with previous studies (e.g. Ezer (2005), Shapiro et al. (2013) and Bruciaferri et al. (2018)). The CUR-*zps* model generates a deeper and less diffused cascade than the one of the GEO-*zps* model, probably due to the increased horizontal resolution of the CUR-*zps* model at the shelf-break.

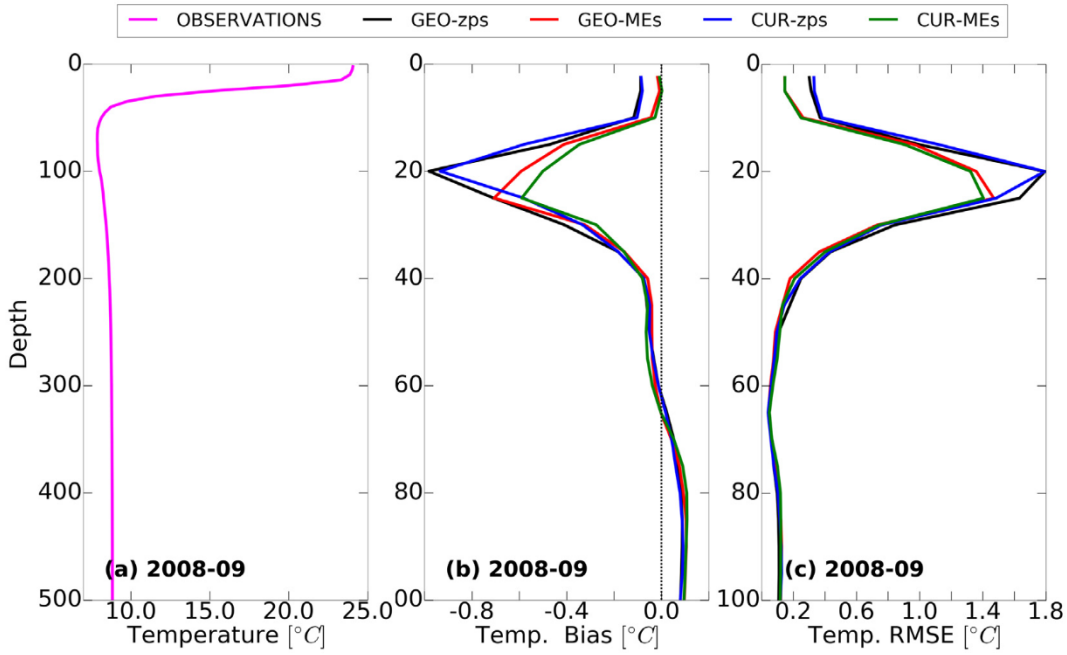

Fig. 6. (a) Basin averaged monthly mean T profile computed by averaging all the available measured profiles of September 2008 with maximum depth ≥ 50 m. (b) Basin averaged vertical profiles of September 2008 mean BIAS of temperature profiles simulated by the four models with respect to observed T profiles. (c) The same of (b) but for the RMSE.

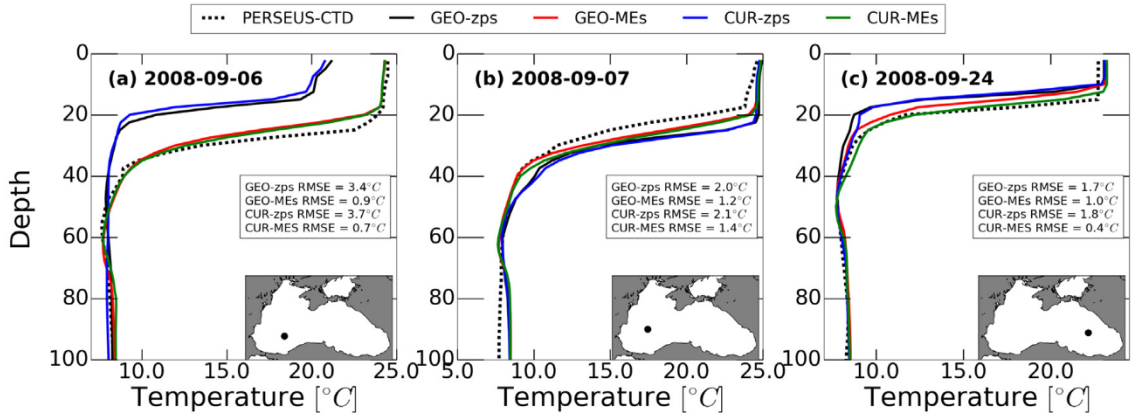

Fig. 7. Comparison between T profiles measured by a CTD profiler (in dashed black) on 2008-09-06 (a), 2008-09-07 (b) and 2008-09-24 (c) and T profiles simulated by GEO-*zps* (black), GEO-ME*s* (red), CUR-*zps* (blue) and CUR-ME*s* (green) models for the same days. The depth-averaged RMSE of the four models with respect to measurements are also given.

The impact of GEO and CUR horizontal grids on the accuracy of the simulation is investigated by comparing satellite detected mesoscale and sub-mesoscale structures in a proximity of the Black Sea north-western shelf and shelf-break during September 2008 with the ones simulated by the four models for the same days (Fig. 9). In general, all models reproduce eddy structures in good agreement with the ones observed by the AVHRR images. However, the increased resolution of the CUR grid in the north-western shelf seems to improve the accuracy of the modelled vortices and mushroom-like features with respect to the regular GEO grid, with spatial and temperature details more similar to the ones observed by the satellite images.

We note that ME*s* based models seem to simulate mesoscale eddies more similar to the ones detected by the satellites. This can be explained considering that on the continental slope the topographic beta effect is the main process affecting the speed of coastal eddies relative to the advection by the mean flow associated with the Rim Current (Stanev and Beckers, 1999a; Staneva et al., 2001). Therefore, *z*-level stepped-topography grid models might reproduce less accurate mesoscale structures due to their difficulties in representing the continental slope and its interaction with the flow, which might result in errors in the simulation of topographic waves, vorticity dynamics and large-scale circulation (e.g. Dukhovskoy et al. (2006), Ezer (2016)).

Results show that the CUR horizontal grid seems to be an additive improvement only when combined with the ME*s* vertical grid. This indicates that the increase of the horizontal resolution in areas where eddy dynamics occurs might improve the accuracy of the simulation only if the model is able to correctly reproduce the underpinning generating mechanisms, i.e. the effect of topography on the flow.

3.2. Comparing the accuracy of the CUR-MEs model and the CMEMS reanalysis

In Section 3.1 the CUR-ME*s* model is proven to be the most accurate model between the four models developed for this study. In EXP-2, we use our CUR-ME*s* model to simulate the 2007–2009 Black Sea

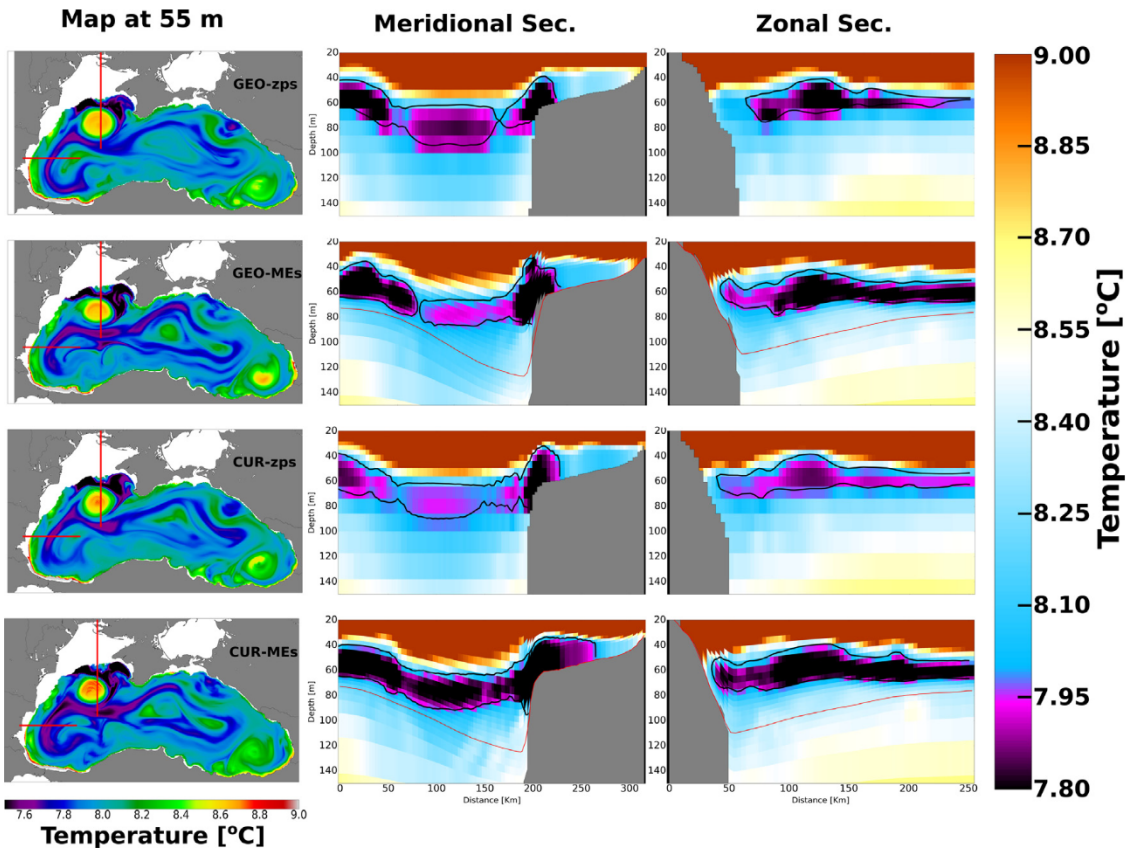

Fig. 8. September 2008 monthly averaged maps at 55 m (*left column*) and meridional (31.7°E, *middle column*) and zonal (42.9°N, *right column*) cross-sections of the Black Sea temperature. In the maps, the red lines show the locations of the cross-sections. In the cross-sections, the thick black lines identify isotherms with $T = 8$ °C while the red lines show the upper envelope H_e^1 of ME*s* models.

circulation and we validate its numerical results against six datasets of measurements. At the same time, we validate data from the CMEMS Black Sea reanalysis against the same set of independent observations and then we compare the accuracy of the two models. The CMEMS model highly assimilates observations and currently represents the best official EU estimate of the 1995–2015 Black Sea state.

We start the analysis by comparing CUR-ME*s* and CMEMS SST daily model outputs with OSTIA SST daily maps (SST from model outputs is retrieved by considering the temperature of the first model level). Fig. 10a shows timeseries of the area averaged SST of OSTIA dataset and simulated by the two models, while Fig. 10b and c present timeseries of BIAS and RMSE, respectively, of CUR-ME*s* and CMEMS model outputs with respect to OSTIA observations.

Numerical results demonstrate that the free-running CUR-ME*s* model and the SST-assimilative CMEMS reanalysis reproduce a seasonal and interannual variability in good agreement with the one of OSTIA observations. Mean metrics show that the CUR-ME*s* model has a mean SST BIAS ≈ 0.3 °C warmer than the one of the CMEMS reanalysis, while the difference between the mean CUR-ME*s* and CMEMS SST RMSE is ≈ 0.6 °C.

The metrics of CUR-ME*s* and CMEMS SST simulations are quite similar in late autumn–winter (November–March period, see Fig. 10b and c), with an average absolute difference between the two models of $\approx$ 0.1 °C for the BIAS and $\approx$ 0.25 °C for the RMSE. In summer, the accuracy of CUR-ME*s* model decreases and mean BIAS and RMSE differences between our free-running model and the CMEMS reanalysis are of ≈ 0.5 °C and ≈ 1.0 °C, respectively. Summer SST overestimation is a known problem of ocean models (see e.g., Ezer (2000) and Hordoir et al. (2018)). It can be attributed to inaccuracies in the atmospheric forcings and/or in the poor representation of the upper ocean mixed layer physics and the SST DA is usually used to improve such model deficiencies (see e.g, O'Dea et al. (2012)).

We continue the comparison of the CUR-ME*s* model and the CMEMS reanalysis by validating their numerical results against five independent datasets of observed T/S profiles (see Section 2.3). Fig. 11 presents timeseries of BIAS and RMSE of salinity (Fig. 11a, b) and temperature (Fig. 11c, d) profiles simulated with the CUR-ME*s* and CMEMS models with respect to in-situ hydrographic profiles.

The CMEMS reanalysis assimilates satellite SST and SLA, T/S profiles and restores T/S fields to their climatological values. CUR-ME*s* model is run in a free mode, without any DA or relaxation to climatology. Nevertheless, the accuracy of the free-running CUR-ME*s* model is very similar to the assimilative CMEMS reanalysis.

Mean metrics shows that the difference between mean salinity BIAS of CUR-ME*s* and CMEMS is 0.07 , while the difference of their mean salinity RMSE is 0.02 . Regarding temperature, the CUR-ME*s* model has a mean BIAS of 0.17 °C colder than the one of CMEMS, while the RMSE of our free-running model is 0.14 °C higher than the one of the CMEMS reanalysis.

A more in depth analysis of monthly timeseries of BIAS and RMSE confirms that the performance of CUR-ME*s* and CMEMS models in simulating salinity field evolution is practically the same. In the case of temperature, they present small differences, mainly concentrated in the summer–autumn period of 2007. The inspection of the actual T profiles simulated with the two models (not shown) reveals that CUR-ME*s* inaccuracies in the last part of 2007 mostly originate in shelf areas, where it is likely that the local stratification still needs to completely recover from the climatological initial condition and where SST errors might significantly affect the thermal properties of the underlying water column.

Fig. 12 presents the basin averaged vertical profiles of the yearly mean salinity and temperature BIAS and RMSE of the CUR-ME*s* model and the CMEMS reanalysis with respect to the observed T/S profiles for

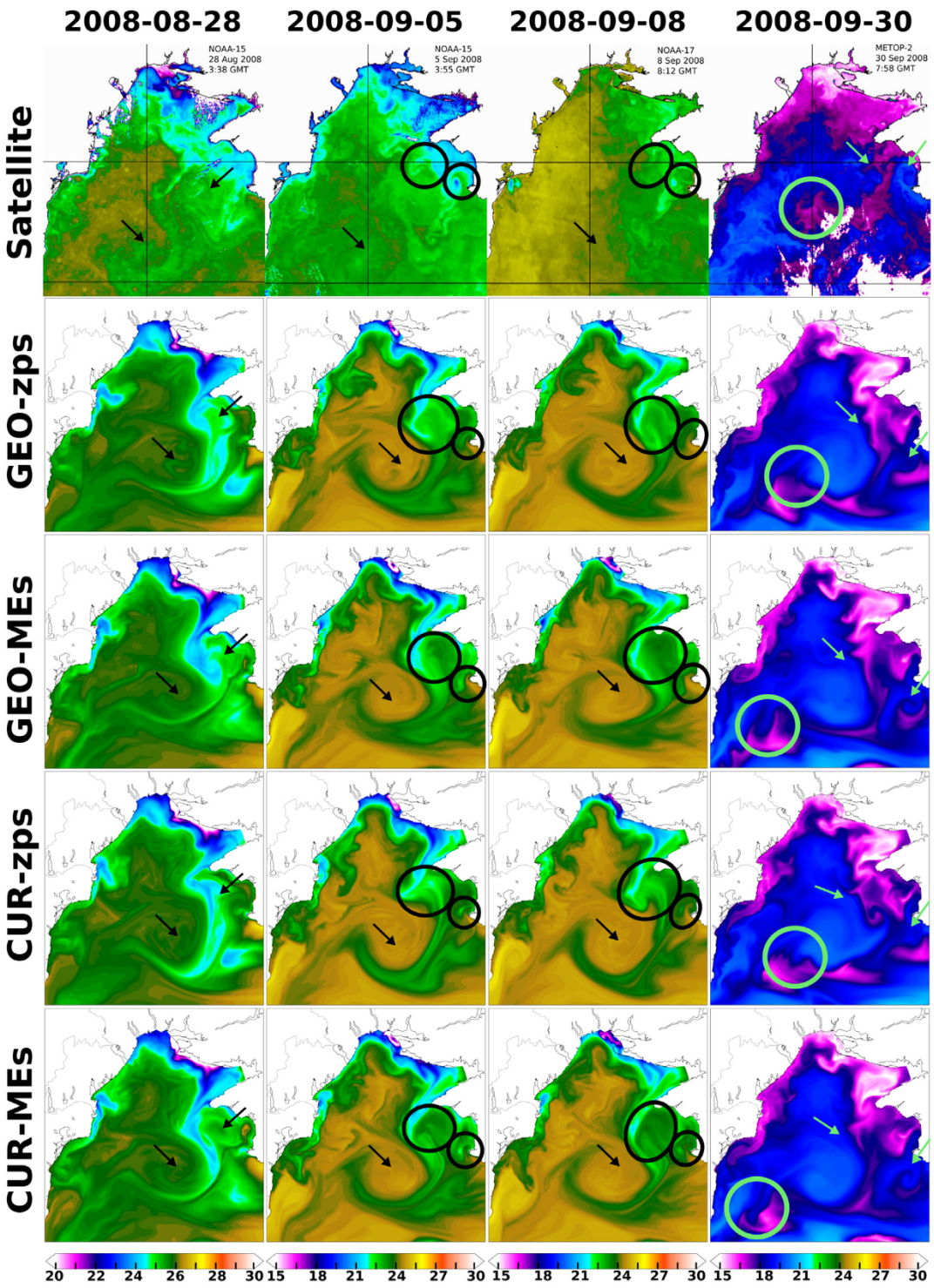

Fig. 9. SST maps detected by AVHRR NOAA and MetOp satellites in a proximity of the Black Sea north-western shelf and shelf-break (*first row*) and daily SST fields simulated by GEO-*zps* (*second row*), GEO-ME*s* (*third row*), CUR-*zps* (*fourth row*) and CUR-ME*s* (*fifth row*) models on 2008-08-28 (*first column*), 2008-09-05 (*second column*), 2008-09-08 (*third* column) and 2008-09-30 (*fourth* column). Arrows and circles identify the mesoscale and sub-mesoscale eddy structures considered for the comparison. SST images are provided by the Remote Sensing Department of the Marine Hydrophysical Institute of RAS (http://dvs.net.ru/mp/data/main.shtml).

2007 (*upper row*), 2008 (*middle row*) and 2009 (*lower row*). The CUR-ME*s* model has greater accuracy (both BIAS and RMSE) in the active CIL layer of the sea (at depths between $\approx$ 35–100 m) in comparison to the CMEMS reanalysis for both salinity and temperature. On the other hand, the SST assimilating CMEMS reanalysis shows a better accuracy in simulating sea surface temperature (at depths between $\approx 0 - 30$ m) while for the sea surface salinity both models seem to be equivalent. Fig. 12 indicates that the warm BIAS of CUR-ME*s* SST (see Fig. 10) and the cold BIAS of both CMEMS and CUR-ME*s* T profiles (see Fig. 11) during summer are probably due to the poor representation of the vertical mixing of the upper layer (0–40 m) of the water column.

3.3. 2007–2009 variability of the Black Sea MKE and CIL

In this section, we use the numerical outputs from the CUR-ME*s* model and the CMEMS reanalysis to study the 2007–2009 seasonal

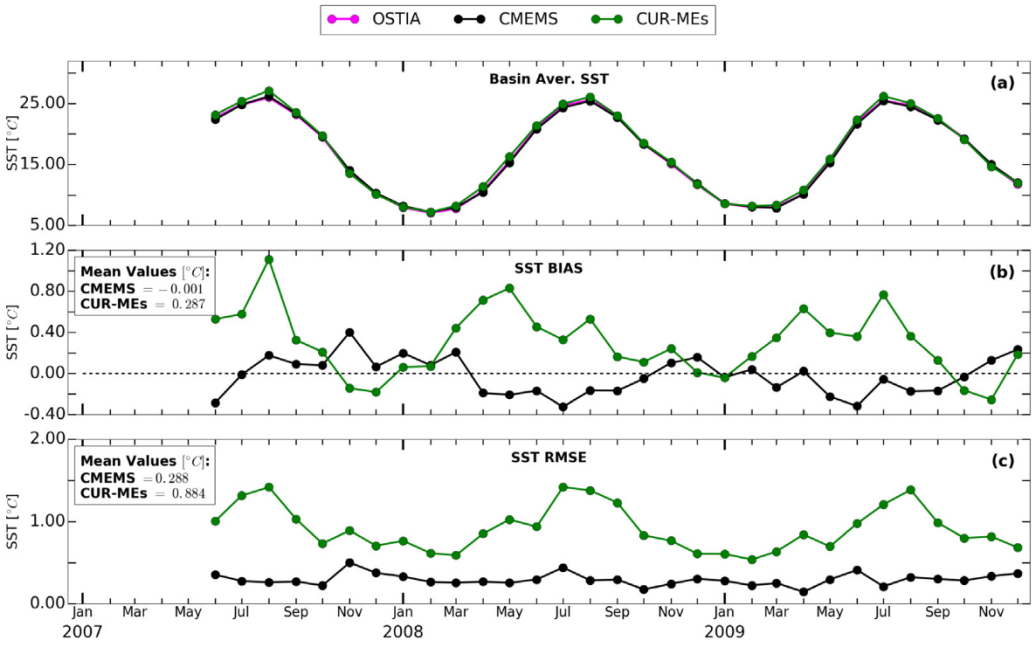

Fig. 10. (a) Monthly timeseries of the area averaged SST retrieved from OSTIA observational dataset (magenta) and simulated by the CUR-ME*s* model (green) and the CMEMS reanalysis (black); (b) Timeseries of the monthly mean BIAS of CUR-ME*s* (green) and CMEMS (black) model outputs with respect to SST OSTIA observations; (c) Timeseries of the monthly mean RMSE of CUR-ME*s* (green) and CMEMS (black) model outputs with respect to SST OSTIA observations. Mean metrics are also given.

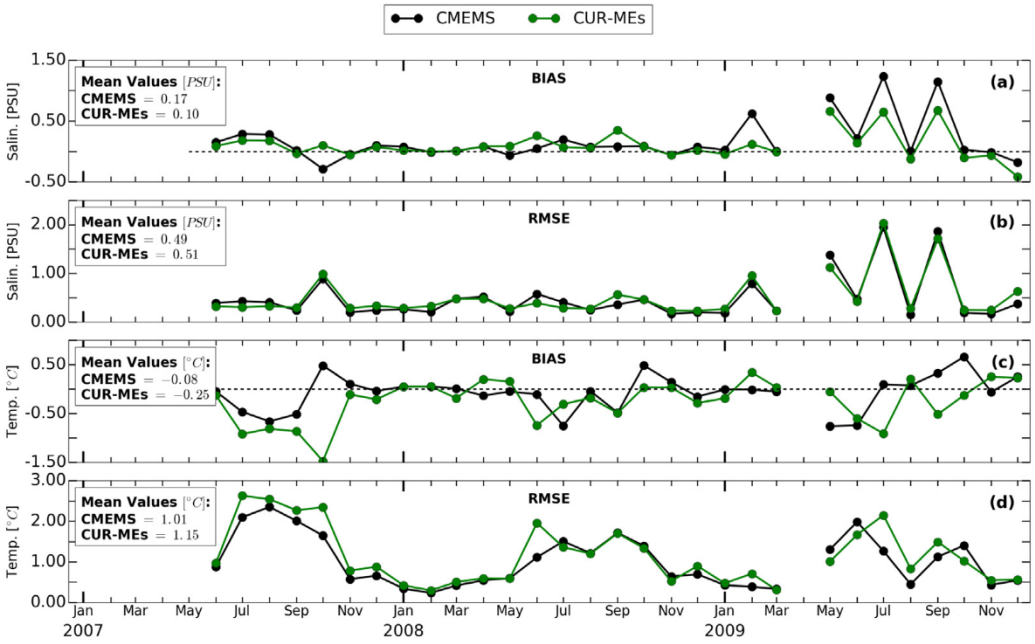

Fig. 11. Monthly timeseries of averaged BIAS and RMSE of salinity (a and b) and temperature (c and d) profiles simulated with the CUR-ME*s* model (green) and by the CMEMS reanalysis (black) with respect to observed T/S profiles. Mean metrics are also given. In May 2009 there are no observations available.

and interannual variability of (i) the Mean Kinetic Energy of currents and (ii) the CIL heat content. Numerical results are compared with observations or with the existing literature.

3.3.1. Mean kinetic energy (MKE) of geostrophic currents

The seasonal and interannual variability of the MKE generated by the geostrophic component of the surface currents averaged over the entire Black Sea surface for the period 2007–2009 is obtained from three sources: (i) the CUR-ME*s* model, (ii) the CMEMS reanalysis and (iii) satellite altimetry data presented in Kubryakov and Stanichny (2015).

The MKE is computed as

$$MKE = \frac{1}{2}(\langle u_g^2 \rangle + \langle v_g^2 \rangle) \tag{2}$$

where $\langle \bullet \rangle$ is an area averaging operator (Kubryakov and Stanichny, 2015). The zonal and meridional components of the geostrophic currents are defined by the geostrophic balance

$$u_g = -\frac{g}{f}\frac{\partial \eta}{\partial y} \tag{3}$$

$$v_g = \frac{g}{f}\frac{\partial \eta}{\partial x} \tag{4}$$

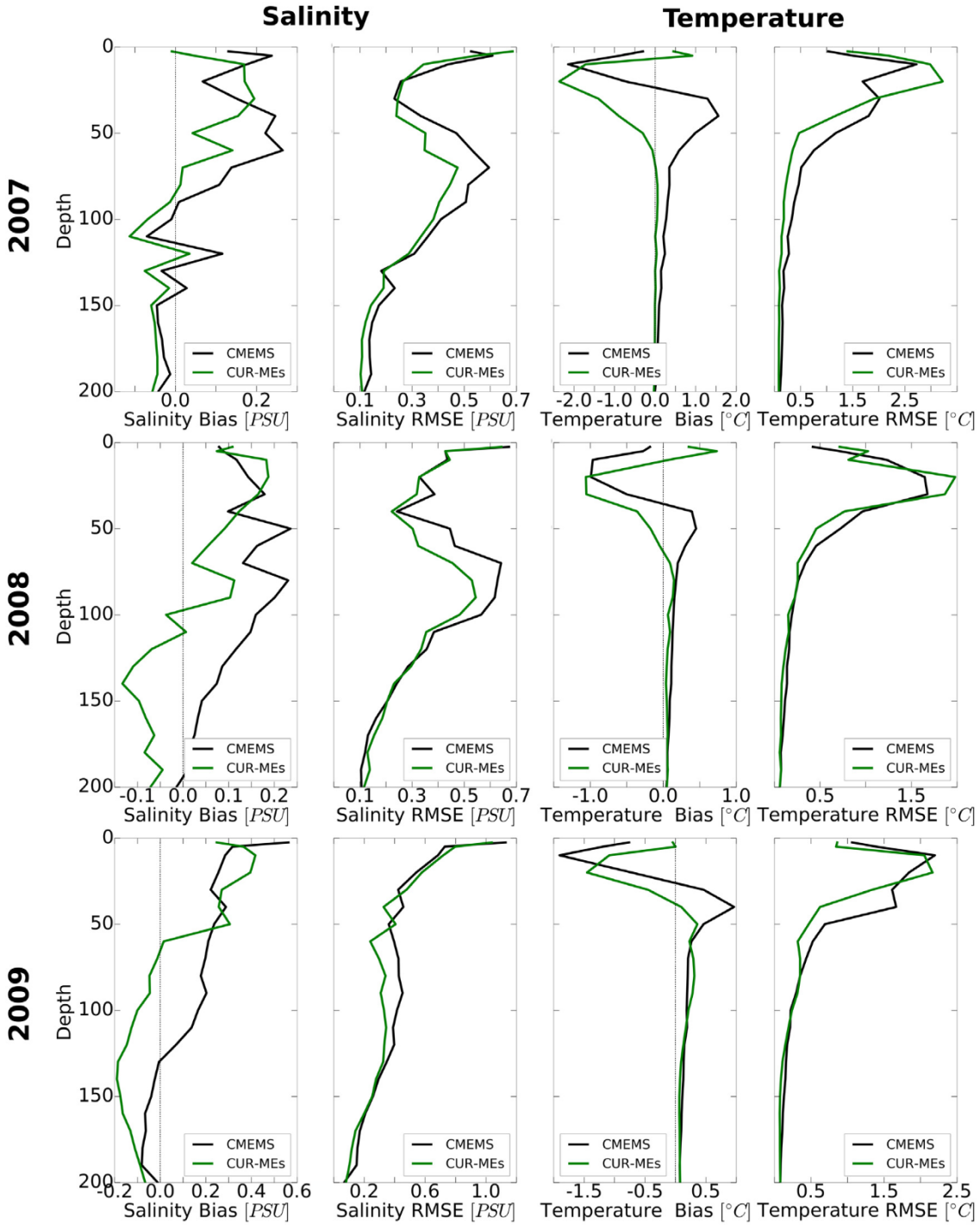

Fig. 12. Basin averaged vertical profiles of yearly mean BIAS and RMSE of salinity and temperature profiles simulated with the CUR-ME*s* model (green) and by the CMEMS reanalysis (black) with respect to observed T/S profiles for 2007 (*upper row*), 2008 (*middle row*) and 2009 (*lower row*).

where g is the gravitational acceleration, f is the Coriolis parameter, η is the Sea Surface Height (SSH) and x and y are the zonal and meridional directions, respectively. In the case of geostrophic currents computed from satellite measurements, the SSH is given by $\eta = MDT + SLA$, where MDT is the 1999–2007 mean dynamic topography calculated by Kubryakov and Stanichny (2011) and SLA is the Sea Level Anomalies field from satellite altimetry (Kubryakov and Stanichny, 2015).

Fig. 13 presents monthly timeseries of the MKE simulated with the CUR-ME*s* and the CMEMS reanalysis models together with the MKE of Kubryakov and Stanichny (2015). The CUR-ME*s* MKE monthly timeseries starts in June 2007 because of the five months spin-up. The variability of the MKE simulated with the CUR-ME*s* model and by the SLA-assimilative CMEMS reanalysis are both in very good agreement with those obtained from satellite observations: the RMSE and correlation coefficient R of our CUR-ME*s* model are 0.004 m^2/s^2 ($\approx$ 20% of the average MKE) and 0.86, respectively, while statistics of the CMEMS reanalysis are RMSE= 0.002 m^2/s^2 ($\approx$ 10% of the average MKE) and R= 0.92.

Both models capture the seasonal MKE cycle, with winter peaks and summer weakening of the large-scale dynamics. Moreover, they also describe a very similar interannual variability, with a more active winter

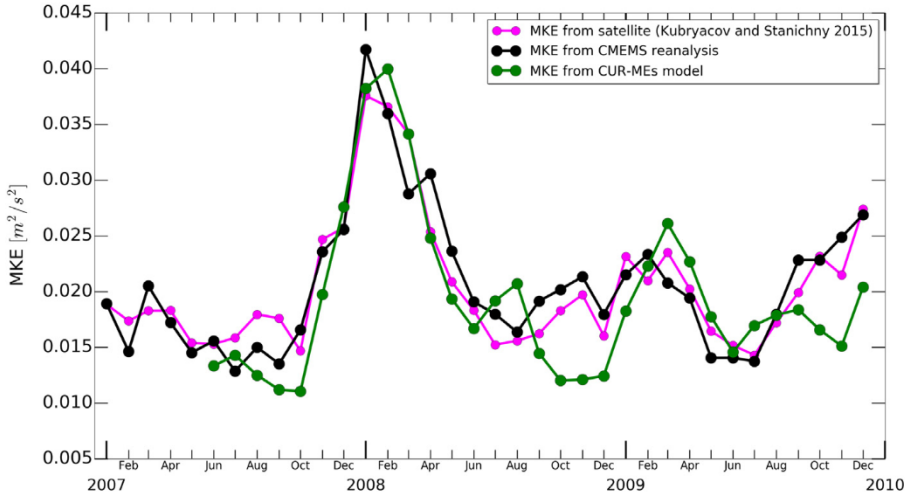

Fig. 13. Monthly timeseries of the MKE simulated with the CUR-ME*s* (green) and CMEMS (black) reanalysis models together with the MKE computed from satellite altimetry observations of Kubryakov and Stanichny (2015) (magenta).

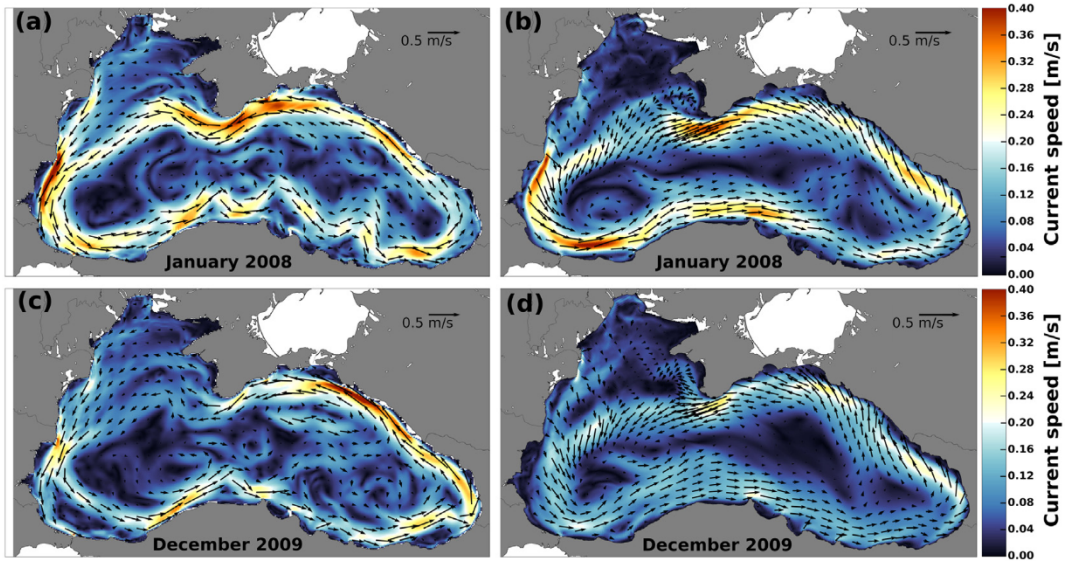

Fig. 14. *January 2008* monthly mean Black Sea surface circulation from (a) the CMEMS reanalysis and (b) the CUR-ME*s* model. *December 2009* monthly mean Black Sea surface circulation from (c) the CMEMS reanalysis and (d) the CUR-ME*s* model.

in 2008 than 2009. The curl of the wind stress is the main forcing of the Rim Current (e.g. Korotaev et al. (2003)). The 2007–2009 timeseries of the basin-averaged wind stress curl over the Black Sea from SKIRON forecast dataset (red line in Fig. 3f) shows a good correlation with the MKE cycle (R= 0.63), proving that the atmospheric forcing adequately represents the 2007–2009 Black Sea wind conditions.

As an example of the winter circulation obtained with the two models, Fig. 14a and b present the January 2008 averaged Black Sea surface circulation simulated with the CMEMS reanalysis and the CUR-ME*s* model, respectively. Both models represent a very similar coherent and well defined Rim Current, flowing along the shelf-break with velocities ranging between 0.2 and 0.4 m/s. They are in good agreement with results presented in other studies, e.g. the January 2008 mean circulation in the upper 30 m of the sea reproduced by the 2000–2012 Black Sea physical reanalysis of the Russian Marine Hydrophysical Institute (MHI) presents a Rim current with velocity between 0.2 and 0.5 m/s (Figure 6a of Sukhikh and Dorofeyev (2016)).

Fig. 14c and d give an example of the autumn Black Sea hydrodynamic reproduced by the two models. They show the December 2009 averaged surface circulation simulated by the CMEMS reanalysis (Fig. 14c) and with the CUR-ME*s* model (Fig. 14d). Both models represent a Rim Current recovering from the summer weakening. The circulation simulated by the two models on the north-western shelf and in front of the Crimean peninsula is similar, with current velocities ranging between 0.15 and 0.25 m/s. Those are the areas where the CUR-ME*s* model has increased horizontal resolution, demonstrating that the usage of the CUR grid allows to achieve an accuracy comparable to the one of the CMEMS reanalysis. In the south-eastern part of the basin, the horizontal resolution of the CUR-ME*s* model is not as high and this seems to affect the accuracy of the model, resulting in slower currents in the Batumi area and along Caucasian coasts. This lower resolution in the south-eastern part of the domain and the possible presence of inaccuracies in the meteorological forcing might explain the CUR-ME*s* underestimation of the Black Sea MKE in autumn in comparison to the one from satellite or CMEMS (Fig. 13).

In Fig. 15, the surface geostrophic circulation for the 16th of April 2008 computed from altimetry data by Kubryakov et al. (2016) (15a) is compared with the daily averaged Black Sea surface circulation simulated with the CMEMS reanalysis (15b) and the CUR-ME*s* model (15c) for the same day. The circulation simulated by the CUR-ME*s*

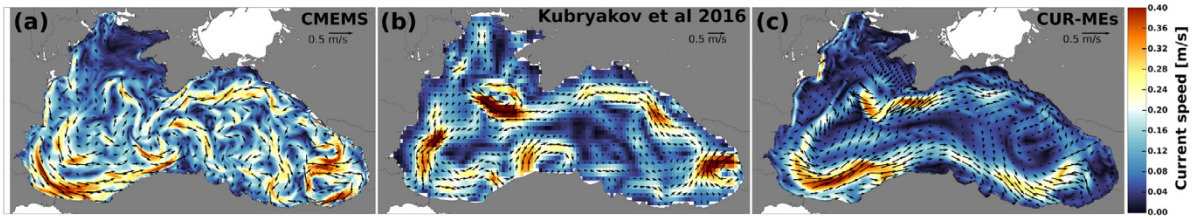

Fig. 15. The Black Sea surface circulation for the 16th of April 2008. (a) Daily mean Black Sea surface circulation from the CMEMS reanalysis. (b) Surface geostrophic currents reconstructed from altimetry data, redrawn after Kubryakov et al. (2016). (c) Daily mean Black Sea surface circulation simulated with the CUR-ME*s* model.

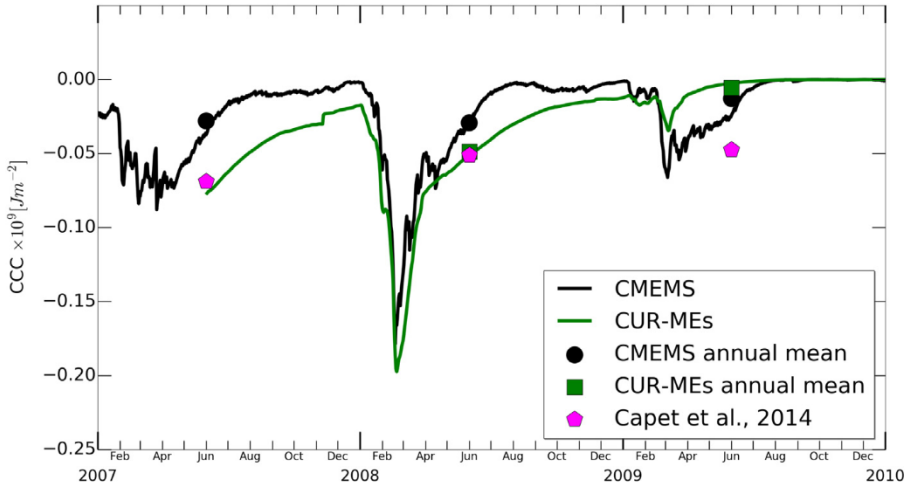

Fig. 16. Daily timeseries of the 2007–2009 basin averaged CCC according to the CUR-ME*s* model (green line) and the CMEMS reanalysis (black line). CCC annual mean values of the CMEMS reanalysis (black circle) and the CUR-ME*s* model (green square) together with annual data redrawn from Capet et al. (2014) (magenta pentagon) are also shown.

model is very similar to the one retrieved from satellite observations on the north-western part of the basin, particularly in a proximity of the Sevastopol anticyclonic eddy and along Crimean coasts, while currents are slower in the south-eastern part, especially in the Batumi area. On the other hand, the circulation given by the CMEMS reanalysis reproduces a Batumi eddy very similar to the one of Kubryakov et al. (2016) calculations, while in a proximity of the Crimean peninsula it describes weaker currents, particularly for the quasi-permanent anticyclonic eddy in front of Sevastopol.

3.3.2. Cold intermediate layer

The 2007–2009 seasonal and interannual variability of the Black Sea CIL is analysed in terms of the temporal evolution of the basin averaged CIL Cold Content (Stanev et al., 2003).

The CIL Cold Content [J m^{-2}] (hereafter CCC) is computed as

$$CCC = \begin{cases} \int_{CIL} c\rho(T - T_r)dz & \text{, if } T \le T_r \text{ and } \rho > 1014 \\ 0 & \text{, if } T > T_r \text{ or } \rho \le 1014 \end{cases} \quad (5)$$

where $c(z)$ is the specific heat capacity [J kg^{-1} K^{-1}], $\rho(z)$ is the sea water density [kg m^{-3}], $T(z)$ is the water temperature [°C] and $T_r = 8$ °C is the reference temperature historically used to identify the CIL (Ivanov and Belokopytov, 2012). The vertical integration is limited by the 8 °C isotherms and it is performed only in areas where density $\rho > 1014$ kg m^{-3} (Stanev et al., 2003).

Fig. 16 presents daily timeseries and annual mean values of the 2007–2009 basin averaged CCC computed using daily model outputs from the CUR-ME*s* model and the CMEMS reanalysis, respectively. The CUR-ME*s* timeseries starts from the 1st of June 2007 because of the five months spin-up. For model-data intercomparison, the annual mean CCC values calculated by Capet et al. (2014) are shown as well. They were computed using Black Sea temperature profiles with depths > 50 m for the period 1955–2011 extracted from the World Ocean Database and applying the Data Interpolating Variational Analysis (DIVA) and Eq. (5) (Capet et al., 2014).

A typical seasonal variability is reproduced by both models, with CIL formation at the beginning of each year and CIL horizontal mixing in summer–autumn. However, CCC annual mean values of the CMEMS reanalysis systematically underestimate the Black Sea CCC given by Capet et al. (2014), with an absolute error of ≈ 0.05 J m^{-2} in 2007, ≈ 0.025 J m^{-2} in 2008 and ≈ 0.035 J m^{-2} in 2009. On the other hand, CUR-ME*s* annual averages show a very good agreement with Capet et al. (2014) estimations in 2008 (error < 0.01 J m^{-2}), while in 2009 our model also underestimates CCC (error ≈ 0.04 J m^{-2}).

In order to better characterize the CIL seasonal and interannual variability, in Fig. 17 the temporal evolution of the monthly mean basin averaged temperature profile for the upper 100 m of the Black Sea according to CMEMS and CUR-ME*s* numerical simulations is shown. Qualitative model-data intercomparison is performed with results from Akpinar et al. (2017) and Stanev et al. (2019), where weekly Argo float T/S profiles are analysed to characterize the meso-scale and monthly-to-interannual variability of the CIL in the periods 2002–2015 (Akpinar et al., 2017) and 2005–2019 (Stanev et al., 2019).

In 2007, the volume of the CIL simulated by the CMEMS reanalysis drastically reduces after July, to such a level that its signal disappears from summer–autumn basin averaged temperature profiles. On the other hand, the CUR-ME*s* model represents a well defined 2007 CIL with depths ranging between 30–100 m until November. This seems to be in good agreement with Akpinar et al. (2017) and Stanev et al. (2019) data, where the existence of a distinct CIL located at depths between 40 − 110 m in the west-central interior basin and in the southeast basin of the Black Sea from March to November–December 2007 is documented.

In 2008, both the CUR-ME*s* model and the CMEMS reanalysis reproduce a quite important CIL replenishment event in January-March, with

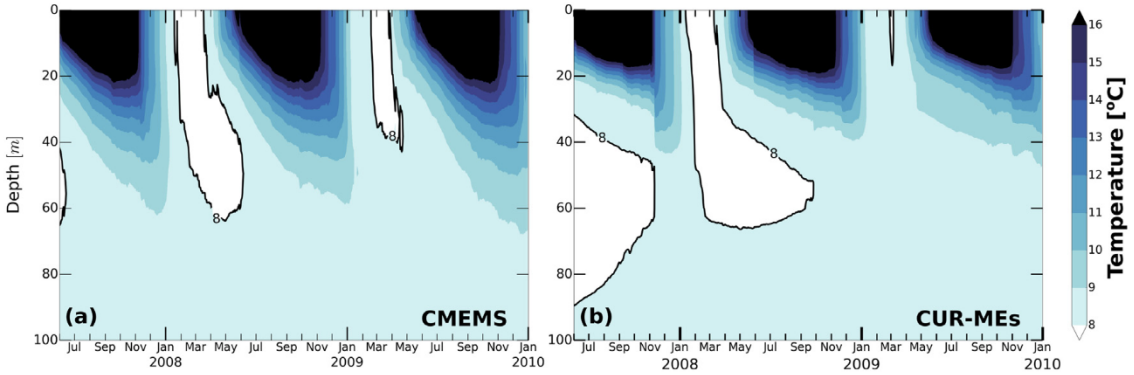

Fig. 17. Time versus depth plot of monthly mean basin averaged temperature profiles [°C] of the upper 100 m of the Black Sea according to the CMEMS reanalysis (a) and the CUR-ME*s* (b) numerical simulations. The thick black lines identify the CIL (water with temperature lower than 8 °C).

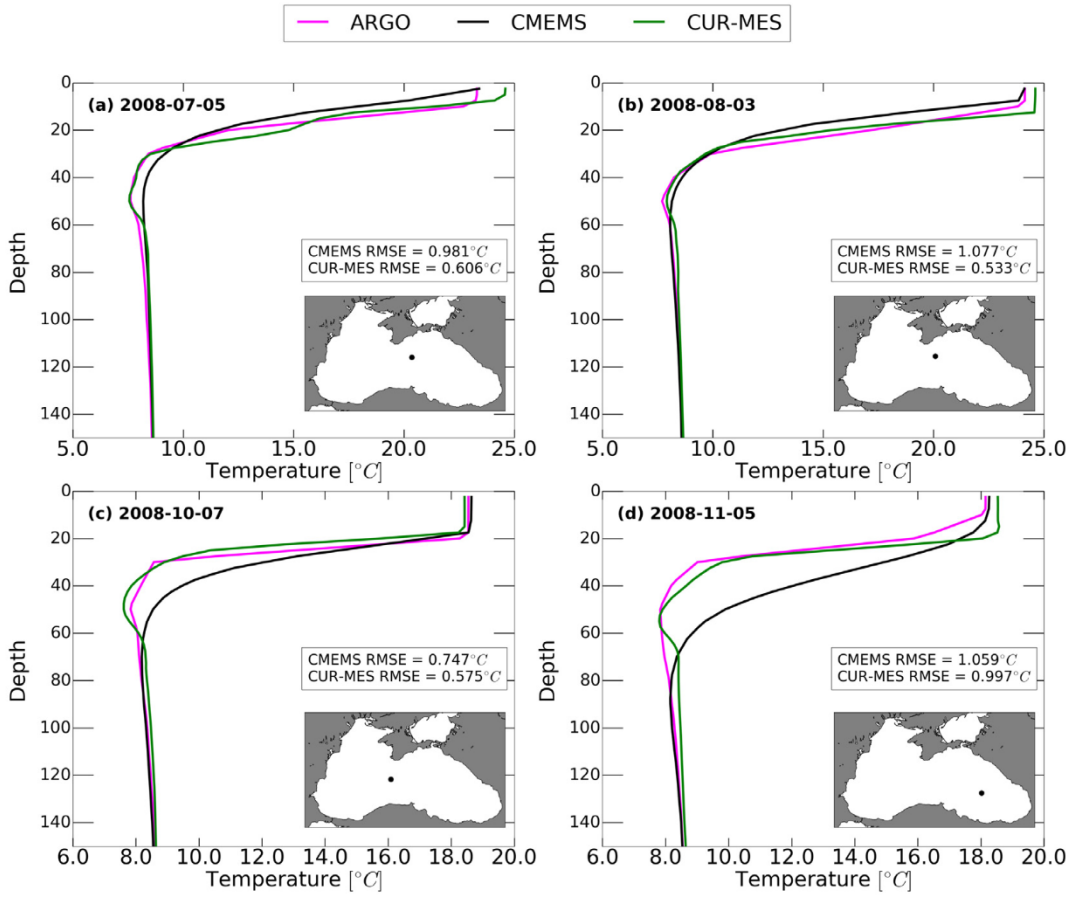

Fig. 18. Comparison between T profiles measured by Argo profilers (in magenta) in summer (18a and b) and autumn (18c and d) and T profiles simulated by CMEMS (black) and CUR-ME*s* (green) models for the same day. The day of the measurement is indicated in the upper-left corner of each sub-panel while the location of the observation is shown in the inset map. RMSE of CMEMS and CUR-ME*s* models with respect to measurements are also given.

strong convection reaching depths of about 60 m. The observational studies of Akpinar et al. (2017) and Stanev et al. (2019) report a very similar CIL formation episode in winter 2008, which promoted the deepening of the mixed layer up to a depth of 80 m. In addition, Akpinar et al. (2017) and Stanev et al. (2019) data show that a CIL with depths between 40 – 60 m is maintained in the west-central interior basin and in the southeast basin of the Black Sea until October–December 2008. Similarly, the CUR-ME*s* model shows a well defined CIL with depth between 40–60 m until October–November 2008. To the contrary, 2008 basin averaged temperature profiles of the CMEMS reanalysis do not show any CIL after July.

In 2009, both the CUR-ME*s* model and the CMEMS reanalysis describe a short replenishment event in March, with a weak winter convective cooling which is not able to maintain the CIL structure for the rest of the year. While there are no data for 2009 in Akpinar et al. (2017), data from Stanev et al. (2019) documents a similar weak replenishment event in March 2009 and a water mass with temperature $\geq$ 8 °C located at depths between 40 m and 80 m until November 2009. Similar results were also obtained by Piotukh et al. (2011), where the authors analysed the 1982–2008 CIL heat content by using CTD observations carried out in the NE part of the Black Sea. In addition, Sukhikh and Dorofeyev (2016) results obtained by

the Russian MHI 2000–2012 Black Sea physical reanalysis also show a similar CIL dynamic for 2009, with weak CIL formation in March and no CIL for the rest of the year. The CUR-ME*s* model reproduces a shorter and weaker CIL formation event in comparison to the other two reanalysis models, probably due to inaccuracies in the heat fluxes of the atmospheric forcing.

Results presented in Figs. 12, 16 and 17 suggest that the CMEMS reanalysis might be affected with too high diapycnal mixing in the active sub-surface layer of the Black Sea, which could explain the disappearing of the CIL signal after July in 2007 and 2008, followed by the autumn formation of the water mass with temperatures between $9-10$ °C in the sub-surface layer ($40-60$ m).

In Fig. 18 we present examples of T profiles measured by the Argo profilers in summer (18a and b) and autumn (18c and d) 2008 compared with T profiles simulated by CMEMS and CUR-ME*s* models for the same day. They clearly confirm the tendency of the CMEMS Reanalysis to over-mix waters between 30 and 100 m, causing a premature summer disappearing of the CIL and the formation of a too warm ($\approx 1-2$ °C) sub-surface active layer.

On the other hand, Fig. 18 further demonstrates the good agreement of CUR-ME*s* model results with observational data, indicating that our multi-scale model, without any DA, is able to correctly reproduce the formation and spreading of the CIL, with limited undesired diapycnal mixing between the surface layer and the CIL.

4. Conclusion

In this paper, we have developed four ocean models for the Black Sea which use the same codebase (NEMO v3.6-stable) and the same initial conditions and external forcing. The only difference is in the discretization schemes, both in the vertical and horizontal directions. One of the models uses the standard z-partial steps in the vertical and lat/lon discretization in the horizontal. The other three models use bespoke schemes with curved grid cells and are designed to better capture important physical processes specific to the Black Sea: instability of the Rim Current, meso- and sub-mesoscale eddies, steep continental slope outside the shelf break and CIL variability. Similar features are also present in other regional seas of the World Ocean.

Inter-comparison of the models shows that the CUR-ME*s* model, which uses grid cells optimized for the main physical processes in all the three directions, has the highest accuracy. In the specific, results show that the vertical grid of the CUR-ME*s* model, which has computational levels nearly following isopycnal surfaces and increased resolution in the active layer of the sea (i.e., at depths between 5 and 100 m), is able to reduce spurious numerical diapycnal mixing improving the representation of the CIL dynamics.

Further comparison of the CUR-ME*s* model with the CMEMS reanalysis shows that the CUR-ME*s* model in a free-run and without relaxation to climatology produces similar and sometimes even better simulation of observed data than the highly assimilative CMEMS reanalysis which currently is considered as a reference for the state of the Black Sea. The difference between the mean BIAS and RMSE of the two models with respect to independent observations is ≈ 0.15 °C for temperature and ≈ 0.07 for salinity. Basin averaged annual mean profiles of the same metrics show that the CMEMS reanalysis, which assimilates SST, has better accuracy in simulating the temperature of the upper layer, while the CUR-ME*s* model presents higher accuracy (both BIAS and RMSE) in the active CIL layer of the sea.

The use of CUR-ME*s* even without DA reveals the details of the inter- and intra-annual variability of the Mean Kinetic Energy. It captures the effect of the warming and weakening of the CIL, which was indicated in some recent observations and allowed us to study this process with high granularity. The highly accurate results obtained with CUR-ME*s* might suggest that a future use of this model in operational forecasting systems would potentially require less intensive DA, being computationally more efficient.

This study proves the skills of the CUR-ME*s* model for 3-years long simulations. A next step would be to apply this new model for longer climate-type runs, to assess whether such a vertical grid optimized for the current oceanic state of the Black Sea may also be appropriate for future scenarios. One possibility is that, under long-term changes of the thermohaline state of the sea, ME*s* computational levels might not mimic anymore the stratification of the basin. This could result in undesired numerical diapycnal mixing, as it is the case for all the other non-isopycnic vertical coordinate system. While the increased resolution of ME*s* levels near the active layer of the sea might alleviate this issue, a further improvement of the ME*s* scheme could be the development of an arbitrary Lagrangian–Eulerian ME*s*-coordinate system, where envelopes and model levels will be able to move in time adapting to the main baroclinic features of the flow (e.g. combining the ideas of Leclair and Madec (2011) and Hofmeister et al. (2010)).

Declaration of competing interest

The authors declare that they have no known competing financial interests or personal relationships that could have appeared to influence the work reported in this paper.

Acknowledgements

We thank Prof. Emil Stanev and the two anonymous Reviewers for their thorough review of our manuscript and the constructive comments and suggestions that were made, they have greatly contributed to improving the manuscript.

D. Bruciaferri was supported by a University of Plymouth, UK Ph.D. studentship. Dr. A.G. Zatsepin participation in the paper was supported by a state assignment of the Ministry of Science and Higher Education of the Russian Federation, Russia (theme №0149-2019-0004). Prof. T. Ezer was supported by the Center for Coastal Physical Oceanography at Old Dominion University, USA.

Appendix. NEMO governing equations, numerics and parameters

The Black Sea models implemented in this study use the NEMO version 3.6 code (Madec, 2008). It solves the standard set of primitive equations usually applied to describe the motion of geophysical fluids: the incompressible, hydrostatic, Boussinesq approximated Navier–Stokes equations for momentum and volume budgets, the tracer advection/diffusion equations for heat and salinity conservation and a diagnostic nonlinear equation of state for the ocean density. In height coordinate and vector invariant form they can be written as follows:

$$\partial_t \mathbf{u}_h = -(\nabla_h \times \mathbf{u}_h)\times \mathbf{u}_h - \frac{1}{2}\nabla_h |\mathbf{u}_h|^2 - w\partial_z \mathbf{u}_h - f\ \mathbf{k}\times\mathbf{u}_h - \frac{1}{\rho_0}\nabla_h p + \mathbf{D^u} + \mathbf{F^u} \tag{A.1}$$

$$\partial_z p = -\rho\ g \tag{A.2}$$

$$\nabla_h \cdot \mathbf{u}_h + \partial_z w = 0 \tag{A.3}$$

$$\partial_t \theta = -\nabla\cdot(\theta\ \mathbf{u}) + D^\theta + L^\theta + F^\theta \tag{A.4}$$

$$\partial_t S = -\nabla\cdot(S\ \mathbf{u}) + D^S + F^S \tag{A.5}$$

$$\rho = \rho(\theta, S, p) \tag{A.6}$$

where $\mathbf{u} = \mathbf{u}_h + w\,\mathbf{k} = (u, v, w)$ is the ocean flow vector (the subscript h denotes a 2D vector with components in the meridional and zonal directions and $\mathbf{k}$ is the local upward vertical unit vector), z is the height referenced to the geoid, θ is the potential temperature, S the practical salinity and ρ is the potential density. $\nabla_h = (\partial_x, \partial_y, 0)$ represents the 2D differential operator while t is time, ρ_0 is the reference density, p the pressure, f is the Coriolis term and g is the gravitational acceleration. $\mathbf{D^u}$, D^θ and D^S parameterize sub-grid physics for momentum, temperature and salinity. $\mathbf{F^u}$, F^θ and F^S introduce surface forcing terms and L^θ describes the penetration of the radiative heat flux in the water column.

In this study, we use the EOS-80 (UNESCO, 1983) formulation for the equation of state $\rho(\theta, S, p)$ and we parameterize the effect of sub-grid scale features on the large scale motions as follows:

$$\mathbf{D}^{\mathbf{u}} = \nabla_h \cdot \left(A_h \nabla_h \mathbf{u}_h\right) - \Delta_h \left(B_h \Delta_h \mathbf{u}_h\right) + \partial_z \left(A_v \partial_z \mathbf{u}_h\right) \tag{A.7}$$

$$D^{\theta} = \nabla_h \cdot \left(K_h \nabla_h \theta\right) + \partial_z \left(K_v \partial_z \theta\right) \tag{A.8}$$

$$D^{S} = \nabla_h \cdot \left(K_h \nabla_h S\right) + \partial_z \left(K_v \partial_z S\right) \tag{A.9}$$

Here, A_h and B_h are the lateral Laplacian and bi-Laplacian viscosity coefficients, respectively, while K_h is the Smagorinsky (1993) lateral diffusivity coefficient. In this study we use $A_h = 1.2 \cdot 10^2$ [m^2 s^{-1}], $B_h = -4 \cdot 10^7$ [m^4 s^{-1}] and $1 \leq K_h \leq 10$ [m^2 s^{-1}]. Moreover, the second order operator for momentum and active tracers lateral diffusion are aligned with horizontal levels while the viscous fourth-order operator is discretized along model levels. Smagorinsky parameterization is tuned following Shapiro et al. (2013).

A_v and K_v are the vertical viscosity and diffusivity coefficients, respectively. They are computed using the Generic Length Scale (GLS) turbulent closure scheme (Umlauf and Burchard, 2003). After tuning experiments, we use GLS scheme with the following parameters: $k - \varepsilon$ turbulent closure together with the Kantha and Clayson (1994) stability function and the Galperin limit equal to 0.267.

Our Black Sea models have closed lateral boundaries with no-slip condition and parameterize Bosphorus exchanges as a two-layers river. At the surface, the following kinematic boundary condition is applied:

$$w\Big|_{z=\eta} - \partial_t \eta - \mathbf{u}_h\Big|_{z=\eta} \cdot \nabla \eta = E - P - R/A + Q_B + \varepsilon_w \tag{A.10}$$

where η is the deviation of the sea surface from its unperturbed position and $E - P - R/A + Q_B$ represents the freshwater budget defined in terms of water fluxes due to evaporation (E), precipitation (P), river discharge per river mouth's area (R/A) and Bosphorus barotropic transport $Q_B = Q_B^u - Q_B^l$, where Q_B^u and Q_B^l are the upper and lower layer Bosphorus fluxes, respectively. In Eq. (A.10) ε_w represents a correction factor applied to close the freshwater budget. It is computed every time step as

$$\varepsilon_w = \frac{1}{A^*} \int_{A^*} (E - P - R/A + Q_B)\, dA^* \tag{A.11}$$

with A^* the model domain area, and added to the atmospheric $E - P$ flux equally at each node of the mesh.

A non linear free surface formulation is chosen to describe the time evolving air–sea interface η, with the following prognostic equation added to the set of equations solved by the models:

$$\partial_t \eta + \nabla \cdot \int_{-H}^{\eta} \mathbf{u}_h \, dz = -\left(E - P - R/A + Q_B + \varepsilon_w\right) \tag{A.12}$$

The surface dynamic boundary conditions for momentum, heat and freshwater are:

$$\mathbf{F}^{\mathbf{u}} \equiv A_v \partial_z \mathbf{u}_h\Big|_{z=\eta} = \rho_0^{-1} \tau \tag{A.13}$$

$$F^{\theta} \equiv K_v \partial_z \theta\Big|_{z=\eta} = (\rho_0 C_p)^{-1} (Q_{tot} - Q_{sr}) \tag{A.14}$$

$$F^{S} \equiv K_v \partial_z S\Big|_{z=\eta} = S\Big|_{z=\eta} (E - P - R/A + \varepsilon_w) + S_B^l Q_B^l \tag{A.15}$$

where $\tau = (\tau_x, \tau_y)$ is the wind stress, $C_p = 4000$ J kg^{-1} K^{-1} is the ocean specific heat, Q_{tot} and Q_{sr} are the net and solar heat fluxes at the sea surface, respectively, and S_B is the salinity of lower layer Bosphorus flux. The penetration in the water column of the short wave radiation Q_{sr} (L^{θ} term in Eq. (A.4)) is parameterized as follows:

$$I(z) = Q_{sr} \left[R\, e^{-z/\xi_0} + \frac{(1-R)}{3} \left(e^{-z/rr} + e^{-z/gg} + e^{-z/bb}\right) \right] \tag{A.16}$$

$$L^{\theta} \equiv \left(\rho C_p\right)^{-1} \partial_z I \tag{A.17}$$

where $I(z)$ is the downward irradiance, R is a constant defining the fraction of non-penetrating light with ξ_0 specifying the very near surface depth of extinction and bb, gg and rr are chlorophyll dependent attenuation coefficients for wavebands blue (400 – 500 nm), green (500–600 nm) and red (600–700 nm). For the dynamic bottom boundary condition we adopt a log-layer enhanced quadratic bottom friction parameterization with minimum and maximum bottom drag coefficient values equal to $2.5 \cdot 10^{-3}$ and 10^{-1}, respectively.

NEMO solves the primitive equations in a horizontal orthogonal curvilinear coordinate system together with a generalized vertical coordinate $s(x, y, z, t)$. Discretization of the equations is performed on an Arakawa C type structured mesh and the transformation from the continuous coordinate system to the discrete mesh is specified in metric terms e_1, e_2, e_3 (see Madec (2008) for their definition).

For all models, the time-splitting formulation for the non linear free surface is applied, with the baroclinic and barotropic time-steps equal to 200.0 and 6.1 s, respectively. The Asselin time filter parameter is 0.1. The pressure Jacobian scheme together with a leapfrog time scheme for calculation of the hydrostatic pressure gradient term are used. The Total Variance Dissipation (TVD) and Energy and ENstrophy (EEN) conservative schemes are chosen for tracer and momentum advection, respectively.

In models using the z with partial steps vertical discretization scheme, the partial steps parameters are tuned as follows: $e_{3,zps}^{min} = 20.0$ m, $e_{3,zps}^{ratio} = 0.1$, $ppkth = 40.363$ and $ppacr = 9.0$.

References

Akpinar, A., Fach, B.A., Oguz, T., 2017. Observing the subsurface thermal signature of the Black Sea cold intermediate layer with Argo profiling floats. Deep Sea Res. I: Oceanogr. Res. Pap. 124, 140–152. http://dx.doi.org/10.1016/j.dsr.2017.04.002.

Argo, 2018. Argo float data and metadata from Global Data Assembly Centre (Argo GDAC). SEANOE, http://dx.doi.org/10.17882/42182.

Aydoğdu, A., Pinardi, N., Özsoy, E., Danabasoglu, G., Gürses, Ö., Karspeck, A., 2018. Circulation of the Turkish Straits System under interannual atmospheric forcing. Ocean Sci. 14 (5), 999–1019. http://dx.doi.org/10.5194/os-14-999-2018.

Besiktepe, S.T., Lozano, C.J., Robinson, A.R., 2001. On the summer mesoscale variability of the Black Sea. J. Mar. Res. 59 (4), 475–515. http://dx.doi.org/10.1357/002224001762842163.

Blatov, A., Ivanov, V., 1992. Hydrology and Hydrodynamics of the Black Sea Shelf Zone. Naukova Dumka, Kiev, p. 242.

Bleck, R., 1998. Ocean modeling in isopycnic coordinates. In: Chassignet, E.P., Verron, J. (Eds.), Ocean Modeling and Parameterization, NATO ASI Mathematical and Physical Sciences Series, Vol. 516. Kluwer Academic Publishers, Dordrecht, pp. 423–448.

Blokhina, M.D., Afanasyev, Y.D., 2003. Baroclinic instability and transient features of mesoscale surface circulation in the Black Sea: Laboratory experiment. J. Geophys. Res. 108 (C10), 3322. http://dx.doi.org/10.1029/2003JC001979.

Bruciaferri, D., Shapiro, G.I., Wobus, F., 2018. A multi-envelope vertical coordinate system for numerical ocean modelling. Ocean Dyn. 68 (10), 1239–1258. http://dx.doi.org/10.1007/s10236-018-1189-x.

Cannaby, H., Fach, B.A., Arkin, S.S., Salihoglu, B., 2015. Climatic controls on biophysical interactions in the Black Sea under present day conditions and a potential future (A1B) climate scenario. J. Mar. Syst. 141, 149–166. http://dx.doi.org/10.1016/j.jmarsys.2014.08.005.

Capet, A., Barth, A., Beckers, J.-M., Marilaure, G., 2012. Interannual variability of Black Sea's hydrodynamics and connection to atmospheric patterns. Deep Sea Res. II 77–80, 128–142. http://dx.doi.org/10.1016/j.dsr2.2012.04.010.

Capet, A., Stanev, E.V., Beckers, J.-M., Murray, J.W., Grégoire, M., 2016. Decline of the Black Sea oxygen inventory. Biogeosciences 13 (4), 1287–1297. http://dx.doi.org/10.5194/bg-13-1287-2016.

Capet, A., Troupin, C., Carstensen, J., Grégoire, M., Beckers, J.-M., 2014. Untangling spatial and temporal trends in the variability of the Black Sea Cold Intermediate Layer and mixed Layer Depth using the DIVA detrending procedure. Ocean Dyn. 64 (3), 315–324. http://dx.doi.org/10.1007/s10236-013-0683-4.

Chelton, D.B., DeSzoeke, R.A., Schlax, M.G., El Naggar, K., Siwertz, N., 1998. Geographical variability of the first baroclinic rossby radius of deformation. J. Phys. Oceanogr. 28 (3), 433–460. http://dx.doi.org/10.1175/1520-0485(1998)028<0433:GVOTFB>2.0.CO;2.

Ciliberti, S.A., Peneva, E., Storto, A., Kandilarov, R., Lecci, R., Yang, C., Coppini, G., Masina, S., Pinardi, N., 2016. Implementation of Black Sea numerical model based on NEMO and 3DVAR data assimilation scheme for operational forecasting. In: EGU General Assembly Conference Abstracts, Vol. 18. p. 16222.

Crise, A., Kaberi, H., Ruiz, J., Zatsepin, A., Arashkevich, E., Giani, M., Karageorgis, A., Prieto, L., Pantazi, M., Gonzalez-Fernandez, D., Ribera d'Alcalà, M., Tornero, V., Vassilopoulou, V., Durrieu de Madron, X., Guieu, C., Puig, P., Zenetos, A., Andral, B., Angel, D., Altukhov, D., Ayata, S., Aktan, Y., Balcolu, E., Benedetti, F., Bouchoucha, M., Buia, M.-C., Cadiou, J.-F., Canals, M., Chakroun, M., Christou, E.,

Christidis, M., Civitarese, G., Coatu, V., Corsini-Foka, M., Cozzi, S., Deidun, A., Dell'Aquila, A., Dogrammatzi, A., Dumitrache, C., Edelist, D., Ettahiri, O., Fonda-Umani, S., Gana, S., Galgani, F., Gasparini, S., Giannakourou, A., Gomoiu, M.-T., Gubanova, A., Gücü, A.-C., Gürses, Ö., Hanke, G., Hatzianestis, I., Herut, B., Hone, R., Huertas, E., Irisson, J.-O., inibilir, M., Jimenez, J., Kalogirou, S., Kapiris, K., Karamfilov, V., Kavadas, S., Keskin, Ç., Kidey, A., Kocak, M., Kondylatos, G., Kontogiannis, C., Kosyan, R., Koubbi, P., Kušpilić, G., La Ferla, R., Langone, L., Laroche, S., Lazar, L., Lefkaditou, E., Lemeshko, I., Machias, A., Malej, A., Mazzocchi, M.-G., Medinets, V., Mihalopoulos, N., Miserocchi, S., Moncheva, S., Mukhanov, V., Oaie, G., Oros, A., Öztürk, A., Öztürk, B., Panayotova, M., Prospathopoulos, A., Radu, G., Raykov, V., Reglero, P., Reygondeau, G., Rougeron, N., Salihoglu, B., Sanchez-Vidal, A., Sannino, G., Santinelli, C., Secrieru, D., Shapiro, G., Simboura, N., Shiganova, T., Sprovieri, M., Stefanova, K., Streftaris, N., Tirelli, V., Tom, M., Topalolu, B., Topçu, N., Tsagarakis, K., Tsangaris, C., Tserpes, G., Turul, S., Uysal, Z., Vasile, D., Violaki, K., Xu, J., Yüksek, A., Papathanassiou, E., 2015. A MSFD complementary approach for the assessment of pressures, knowledge and data gaps in Southern European Seas: The PERSEUS experience. Mar. Pollut. Bull. 95 (1), 28–39. http://dx.doi.org/10.1016/j.marpolbul.2015.03.024.

Diansky, N.A., Fomin, V.V., Zhokhova, N.V., Korshenko, A.N., 2013. Simulations of currents and pollution transport in the coastal waters of Big Sochi. Izv. Atmos. Ocean. Phys. 49 (6), 611–621. http://dx.doi.org/10.1134/S0001433813060042.

Divinsky, B.V., Kuklev, S.B., Zatsepin, A.G., Chubarenko, B.V., 2015. Simulation of submesoscale variability of currents in the Black Sea coastal zone. Oceanology 55 (6), 814–819. http://dx.doi.org/10.1134/S000143701506003X.

Donlon, C.J., Martin, M., Stark, J., Roberts-Jones, J., Fiedler, E., Wimmer, W., 2012. The operational sea surface temperature and sea ice analysis (OSTIA) system. Remote Sens. Environ. 116, 140–158. http://dx.doi.org/10.1016/j.rse.2010.10.017.

Dukhovskoy, D.S., Morey, S.L., O'Brien, J.J., 2006. Influence of multi-step topography on barotropic waves and consequences for numerical modeling. Ocean Model. 14 (1–2), 45–60. http://dx.doi.org/10.1016/j.ocemod.2006.03.002.

Enriquez, C.E., Shapiro, G.I., Souza, A.J., Zatsepin, A.G., 2005. Hydrodynamic modelling of mesoscale eddies in the Black Sea. Ocean Dyn. 55 (5–6), 476–489. http://dx.doi.org/10.1007/s10236-005-0031-4.

Ezer, T., 2000. On the seasonal mixed layer simulated by a basin-scale ocean model and the Mellor-Yamada turbulence scheme. J. Geophys. Res.: Oceans 105 (C7), 16843–16855. http://dx.doi.org/10.1029/2000JC900088.

Ezer, T., 2005. Entrainment, diapycnal mixing and transport in three-dimensional bottom gravity current simulations using the Mellor–Yamada turbulence scheme. Ocean Model. 9 (2), 151–168. http://dx.doi.org/10.1016/j.ocemod.2004.06.001.

Ezer, T., 2016. Revisiting the problem of the Gulf Stream separation: on the representation of topography in ocean models with different types of vertical grids. Ocean Model. 104, 15–27. http://dx.doi.org/10.1016/j.ocemod.2016.05.008.

Ezer, T., Mellor, G.L., 1994. Diagnostic and prognostic calculations of the North Atlantic circulation and sea level using a sigma coordinate ocean model. J. Geophys. Res. 99 (C7), 14159. http://dx.doi.org/10.1029/94JC00859.

Ezer, T., Mellor, G.L., 2000. Sensitivity studies with the North Atlantic sigma coordinate Princeton Ocean Model. Dyn. Atmos. Oceans 32, 185–208.

Ezer, T., Mellor, G.L., 2004. A generalized coordinate ocean model and a comparison of the bottom boundary layer dynamics in terrain-following and in z-level grids. Ocean Model. 6 (3–4), 379–403. http://dx.doi.org/10.1016/S1463-5003(03)00026-X.

Friedrich, J., Aleynik, D., Kusch, S., Mee, L., Minicheva, G., Shapiro, G., Soloviev, D., Stevens, T., Teaca, A., 2008. Cruise report POS 363 RV "Poseidon" [POS363], March 7 to 25 2008, Varna/Varna. Alfred Wegener Inst. Polar Mar. Res. http://dx.doi.org/10.3289/CR_POS_363.

Grayek, S., Stanev, E.V., Kandilarov, R., 2010. On the response of Black Sea level to external forcing: altimeter data and numerical modelling. Ocean Dyn. 60 (1), 123–140. http://dx.doi.org/10.1007/s10236-009-0249-7.

GRDC, 2014. Global Freshwater Fluxes into the World Oceans - Online provided by Global Runoff Data Centre. Koblenz: Federal Institute of Hydrology (BfG).

Griffies, S.M., 2004. Fundamentals of Ocean Climate Models. Princeton University Press, Princeton, NJ, p. 518.

Gusev, A.V., Zalesny, V.B., Fomin, V.V., 2017. Technique for simulation of Black Sea circulation with increased resolution in the area of the IO RAS polygon. Oceanology 57 (6), 880–891. http://dx.doi.org/10.1134/S0001437017060054.

Hofmeister, R., Burchard, H., Beckers, J.M., 2010. Non-uniform adaptive vertical grids for 3D numerical ocean models. Ocean Model. 33 (1–2), 70–86. http://dx.doi.org/10.1016/j.ocemod.2009.12.003.

Hordoir, R., Axell, L., Höglund, A., Dieterich, C., Fransner, F., Gröger, M., Liu, Y., Pemberton, P., Schimanke, S., Andersson, H., Ljungemyr, P., Nygren, P., Falahat, S., Nord, A., Jönsson, A., Lake, I., Döös, K., Hieronymus, M., Dietze, H., Löptien, U., Kuznetsov, I., Westerlund, A., Tuomi, L., Haapala, J., 2018. Nemo-Nordic 1.0: A NEMO based ocean model for Baltic & North Seas, research and operational applications. Geosci. Model Dev. Discuss. 2018, 1–29. http://dx.doi.org/10.5194/gmd-2018-2.

Ivanov, V.A., Belokopytov, V.N., 2012. Oceanography of the Black Sea. Sevastopol, National Academy of Science of Ukraine, Marine Hydrophysical Institute, p. 210.

Ives, D.C., 1982. Conformal grid generation. Appl. Math. Comput. 10–11, 107–135. http://dx.doi.org/10.1016/0096-3003(82)90189-8.

Kallos, G., Nickovic, S., Papadopoulos, A., Jovic, D., Kakaliagou, O., Misirlis, N., Boukas, L., Mimikou, N., Sakellaridis, G., Papageorgiou, J., Anadranistakis, E. Manousakis, M., 1997. The regional weather forecasting system SKIRON: an overview. In: Proceedings of the International Symposium on Regional Weather Prediction on Parallel Computer Environments, Athens, Greece, pp. 109–122.

Kantha, L.H., Clayson, C.A., 1994. An improved mixed layer model for geophysical applications. J. Geophys. Res. 99 (C12), 25235. http://dx.doi.org/10.1029/94JC02257.

Korotaev, G.K., Knysh, V.V., Kubryakov, A.I., 2014. Study of formation process of cold intermediate layer based on reanalysis of Black Sea hydrophysical fields for 1971–1993. Izv. Atmos. Ocean. Phys. 50 (1), 35–48. http://dx.doi.org/10.1134/S0001433813060108.

Korotaev, G.K., Oguz, T., Dorofeyev, V.L., Demyshev, S.G., Kubryakov, A.I., Ratner, Y.B., 2011. Development of Black Sea nowcasting and forecasting system. Ocean Sci. 7 (5), 629–649. http://dx.doi.org/10.5194/os-7-629-2011.

Korotaev, G.K., Oguz, T., Nikiforov, A., Koblinsky, C.J., 2003. Seasonal, interannual, and mesoscale variability of the Black Sea upper layer circulation derived from altimeter data. J. Geophys. Res. 108 (C4), 3122. http://dx.doi.org/10.1029/2002JC001508.

Kubryakov, A.A., Stanichny, S.V., 2011. Mean Dynamic Topography of the Black Sea, computed from altimetry, drifter measurements and hydrology data. Ocean Sci. 7 (6), 745–753. http://dx.doi.org/10.5194/os-7-745-2011.

Kubryakov, A., Stanichny, S., 2015. Seasonal and interannual variability of the Black Sea eddies and its dependence on characteristics of the large-scale circulation. Deep Sea Res. I: Oceanogr. Res. Pap. 97, 80–91. http://dx.doi.org/10.1016/j.dsr.2014.12.002.

Kubryakov, A.A., Stanichny, S.V., Zatsepin, A.G., Kremenetskiy, V.V., 2016. Long-term variations of the Black Sea dynamics and their impact on the marine ecosystem. J. Mar. Syst. 163, 80–94. http://dx.doi.org/10.1016/j.jmarsys.2016.06.006.

Large, W.G., Yeager, S.G., 2009. The global climatology of an interannually varying air–sea flux data set. Clim. Dynam. 33 (2–3), 341–364. http://dx.doi.org/10.1007/s00382-008-0441-3.

Leclair, M., Madec, G., 2011. z-Coordinate, an Arbitrary Lagrangian-Eulerian coordinate separating high and low frequency motions. Ocean Model. 37 (3–4), 139–152. http://dx.doi.org/10.1016/j.ocemod.2011.02.001.

Lemieux-Dudon, B., Storto, A., Ciliberti, S., Peneva, E., Macchia, F., 2018. Black Sea CMEMS reanalysis - quality information document. Tech. rep.,, p. 3.0, http://marine.copernicus.eu/documents/QUID/CMEMS-BS-QUID-007-004.pdf.

Lishaev, P.N., Knysh, V.V., Korotaev, G.K., 2018. Reproduction of variability of the Black Sea level and pycnocline characteristics based on the adaptive statistics method. Phys. Oceanogr. 25 (4), http://dx.doi.org/10.22449/1573-160X-2018-4-251-261.

Madec, G., 2008. NEMO ocean engine. In: Note du Pôle de Modélisation. Institut Pierre-Simon Laplace (IPSL), p. 357, (27).

Marinova, V., Valcheva, N., 2017. Black Sea CMEMS reprocessed in-situ temperature and salinity - Quality Information Document. Tech. rep.,, p. 1.8, http://cmems-resources.cls.fr/documents/QUID/CMEMS-INS-QUID-013-042.pdf.

Martinho, A.S., Batteen, M.L., 2006. On reducing the slope parameter in terrain-following numerical ocean models. Ocean Model. 13 (2), 166–175. http://dx.doi.org/10.1016/j.ocemod.2006.01.003.

Mee, L.D., 1992. The Black Sea in Crisis: A Need for Concerted International Action. Ambio 21 (4), 278–286.

Miladinova, S., Stips, A., Garcia-Gorriz, E., Macias Moy, D., 2017. Black Sea thermohaline properties: Long-term trends and variations. J. Geophys. Res.: Oceans 122 (7), 5624–5644. http://dx.doi.org/10.1002/2016JC012644.

Miladinova, S., Stips, A., Garcia-Gorriz, E., Macias Moy, D., 2018. Formation and changes of the Black Sea cold intermediate layer. Prog. Oceanogr. 167, 11–23. http://dx.doi.org/10.1016/j.pocean.2018.07.002.

Mizyuk, A.I., Puzina, O.S., Senderov, M.V., 2018. Accuracy of the reconstructed temperature in the Black Sea upper layer from nowcasting/forecasting systems. J. Phys. Conf. Ser. 1128 (1), 12146.

O'Dea, E.J., Arnold, A.K., Edwards, K.P., Furner, R., Hyder, P., Martin, M.J., Siddorn, J.R., Storkey, D., While, J., Holt, J.T., Liu, H., 2012. An operational ocean forecast system incorporating NEMO and SST data assimilation for the tidally driven European North-West shelf. J. Oper. Oceanogr. 5 (1), 3–17. http://dx.doi.org/10.1080/1755876X.2012.1102012.

Pacanowski, R.C., Gnanadesikan, A., Olume, V., 1998. Transient response in a Z - level ocean model that resolves topography with partial cells. Mon. Weather Rev. 126 (12), 3248–3270. http://dx.doi.org/10.1175/1520-0493(1998)126<3248:TRIAZL>2.0.CO;2.

Piotukh, V.B., Zatsepin, A.G., Kazmin, A.S., Yakubenko, V.G., 2011. Impact of the winter cooling on the variability of the thermohaline characteristics of the active layer in the Black Sea. Oceanology 51 (2), 221–230. http://dx.doi.org/10.1134/S0001437011020123.

Shapiro, G.I., 2008. Black Sea Circulation. Encyclopedia Ocean Sci. 401–414. http://dx.doi.org/10.1016/B978-012374473-9.00600-7.

Shapiro, G.I., Luneva, M., Pickering, J., Storkey, D., 2013. The effect of various vertical discretization schemes and horizontal diffusion parameterization on the performance of a 3-D ocean model: the Black Sea case study. Ocean Sci. 9 (2), 377–390. http://dx.doi.org/10.5194/os-9-377-2013.

Shapiro, G.I., Stanichny, S.V., Stanychna, R.R., 2010. Anatomy of shelf-deep sea exchanges by a mesoscale eddy in the North West Black Sea as derived from remotely sensed data. Remote Sens. Environ. 114 (4), 867–875. http://dx.doi.org/10.1016/j.rse.2009.11.020.

Shapiro, G.I., Wobus, F., Aleynik, D.L., 2011. Seasonal and inter-annual temperature variability in the bottom waters over the western Black Sea shelf. Ocean Sci. 7 (5), 585–596. http://dx.doi.org/10.5194/os-7-585-2011.

Shom, 2018. EMODnet Digital Bathymetry (DTM 2018). http://dx.doi.org/10.12770/18ff0d48-b203-4a65-94a9-5fd8b0ec35f6, Shom (Service Hydrographique et Océanographique de la Marine).

Sikirić, M.D., Janeković, I., Kuzmić, M., 2009. A new approach to bathymetry smoothing in sigma-coordinate ocean models. Ocean Model. 29 (2), 128–136. http://dx.doi.org/10.1016/j.ocemod.2009.03.009.

Smagorinsky, J., 1993. Large eddy simulation of complex engineering and geophysical flows. In: Galperin, B., Orszag, S. (Eds.), Evolution of Physical Oceanography. Cambridge University Press, pp. 3–36.

Stanev, E.V., 2005. Understanding Black Sea Dynamics: Overview of Recent Numerical Modeling. Oceanography 18 (2), 56–75. http://dx.doi.org/10.5670/oceanog.2005.42.

Stanev, E.V., Beckers, J., 1999a. Barotropic and baroclinic oscillations in strongly stratified ocean basins. J. Mar. Syst. 19 (1–3), 65–112. http://dx.doi.org/10.1016/S0924-7963(98)00024-4.

Stanev, E.V., Beckers, J.-M.M., 1999b. Numerical simulations of seasonal and interannual variability of the Black Sea thermohaline circulation. J. Mar. Syst. 22 (4), 241–267. http://dx.doi.org/10.1016/S0924-7963(99)00043-3.

Stanev, E.V., Bowman, M.J., Peneva, E.L., Staneva, J.V., 2003. Control of Black Sea intermediate water mass formation by dynamics and topography: Comparison of numerical simulations, surveys and satellite data. J. Mar. Res. 61 (1), 59–99. http://dx.doi.org/10.1357/002224003321586417.

Stanev, E.V., Grashorn, S., Zhang, Y.J., 2017. Cascading ocean basins: numerical simulations of the circulation and interbasin exchange in the Azov-Black-Marmara-Mediterranean Seas system. Ocean Dyn. 67 (8), 1003–1025. http://dx.doi.org/10.1007/s10236-017-1071-2.

Stanev, E.V., He, Y., Staneva, J., Yakushev, E., 2014. Mixing in the Black Sea detected from the temporal and spatial variability of oxygen and sulfide – Argo float observations and numerical modelling. Biogeosciences 11 (20), 5707–5732. http://dx.doi.org/10.5194/bg-11-5707-2014.

Stanev, E.V., Peneva, E., Chtirkova, B., 2019. Climate change and regional ocean water mass disappearance: Case of the Black Sea. J. Geophys. Res.: Oceans http://dx.doi.org/10.1029/2019JC015076, 2019JC015076.

Stanev, E., Roussenov, V., Rachev, N., Staneva, J., 1995. Sea response to atmospheric variability. Model study for the Black Sea. J. Mar. Syst. 6 (3), 241–267. http://dx.doi.org/10.1016/0924-7963(94)00026-8.

Stanev, E.V., Staneva, J.V., Roussenov, V.M., 1997. On the Black Sea water mass formation. Model sensitivity study to atmospheric forcing and parameterizations of physical processes. J. Mar. Syst. 13 (1–4), 245–272. http://dx.doi.org/10.1016/S0924-7963(96)00115-7.

Staneva, J.V., Dietrich, D.E., Stanev, E.V., Bowman, M.J., 2001. Rim current and coastal eddy mechanisms in an eddy-resolving Black Sea general circulation model. J. Mar. Syst. 31 (1–3), 137–157. http://dx.doi.org/10.1016/S0924-7963(01)00050-1.

Staneva, J.V., Stanev, E.V., Rachev, N.H., 1995. Heat balance estimates using atmospheric analysis data: A case study for the Black Sea. J. Geophys. Res 100 (C9), 518–581. http://dx.doi.org/10.1029/95JC01851.

Sukhikh, L., Dorofeyev, V., 2016. The study of sensitivity of the Black Sea hydrophysical fields reanalysis results to the applied atmospheric forcing. Phys. Oceanogr. (5), http://dx.doi.org/10.22449/1573-160X-2016-5-45-60.

Suvorov, A., Palmer, D., Khaliulin, A., Godin, E., Belokopytov, V., 2003. Digital atlas and evaluation of the influence of inter-annual variability on climate analyses. In: Oceans 2003. Celebrating the Past ... Teaming Toward the Future (IEEE Cat. No.03CH37492), Vol. 2. IEEE, pp. 990–995. http://dx.doi.org/10.1109/OCEANS.2003.178468.

Umlauf, L., Burchard, H., 2003. A generic length-scale equation for geophysical turbulence models. J. Mar. Res. 61 (2), 235–265. http://dx.doi.org/10.1357/002224003322005087.

UNESCO, 1983. Algorithms for computation of fundamental property of sea wa- ter.. Techn. Paper in Mar. Sci 44.

Vespremeanu, E., Golumbeanu, M., 2018. Black Sea Coastal Population. In: The Black Sea. Springer International Publishing, pp. 115–124. http://dx.doi.org/10.1007/978-3-319-70855-3.

Xu, S., Wang, B., Liu, J., 2015. On the use of Schwarz–Christoffel conformal mappings to the grid generation for global ocean models. Geosci. Model Dev. 8 (10), 3471–3485. http://dx.doi.org/10.5194/gmd-8-3471-2015.

Zatsepin, A.G., Ginzburg, A.I., Kostianoy, A.G., Kremenetskiy, V.V., Krivosheya, V.G., Stanichny, S.V., Poulain, P., 2003. Observations of Black Sea mesoscale eddies and associated horizontal mixing. J. Geophys. Res. 108 (C8), 3246. http://dx.doi.org/10.1029/2002JC001390.

Zatsepin, A., Kubryakov, A., Aleskerova, A., Elkin, D., Kukleva, O., 2019. Physical mechanisms of submesoscale eddies generation: evidences from laboratory modeling and satellite data in the Black Sea. Ocean Dyn. 69 (2), 253–266. http://dx.doi.org/10.1007/s10236-018-1239-4.

Zhou, F., Shapiro, G.I., Wobus, F., 2014. Cross-shelf exchange in the northwestern Black Sea. J. Geophys. Res.: Oceans 119 (4), 2143–2164. http://dx.doi.org/10.1002/2013JC009484.